Zinc-substituted Ag_2CrO_4: a material with enhanced photocatalytic and biological activity

Ivo M. Pinatti [a], Ana C. M. Tello [a], Aline B. Trench [a], Camila C. de Foggi [a], Paula F. S. Pereira [a], Mayara M. Teixeira [a], Natalia Jacomaci [b], Juan Andrés [c], and Elson Longo [a*]

[a] *CDMF, LIEC, Federal University of São Carlos, P.O. Box 676, São Carlos 13565-905, Brazil.*

[b] *LIEC, Institute of Chemistry, São Paulo State University "Júlio Mesquita Filho" (UNESP), Araraquara, Brazil.*

[c] *Department of Analytical and Physical Chemistry, University Jaume I (UJI), Castelló 12071, Spain.*

**corresponding author: elson.liec@gmail.com*

Abstract

In the past years, new environmentally-friendly photocatalysts have been reported, but the realization of efficient visible-light driven photocatalyst with highly active bactericidal and fungicidal activity is still challenging. This work is a joint experimental and theoretical study on the structural, electronic, and optical properties of Ag_2CrO_4:Zn^{2+} (ACOxZn, x = 1%, 2%, and 4%) solid solutions for photocatalytic, bactericidal, and fungicidal activity. For the first time, synthesis of these innovative and multifunctional materials were performed through the cation exchange of zinc and silver using a simple, fast, and cheap co-precipitation method. Powder X-ray diffraction measurements revealed the long range order of the materials. X-ray photoelectron spectroscopy provided information about the surface of the samples demonstrating that they were pure. The materials showed short-range order as verified by FT-Raman spectroscopy. Additionally, ultraviolet-visible diffuse reflectance spectra and photoluminescence spectroscopy were used to examine the electronic properties which corroborated with the increasing photocatalytic activity for the degradation of Rhodamine B and bactericidal activity against *Staphylococcus aureus* and *Candida albicans*. Field emission scanning electron microscopy images showed different types of particles with different facets and sizes. Theoretical results based on density functional theory calculations complement the experimental results to rationalize the effects of the incorporation of Zn cations in the ACO host lattice.

Introduction

Development of new visible-light photocatalysts with enhanced performance for meeting the global energy demand is still challenging. Additionally, an increase in the concentration of phenols, pesticides, dyes, solvents, and other organic pollutants with potentially carcinogenic activities in wastewater was recently observed. The photocatalytic (PC) decomposition of these pollutants under visible light is a promising emerging alternative approach for wastewater treatment because it utilizes solar energy and does not produce secondary products since the organic materials are decomposed into non-toxic molecules such as H_2O, CO_2, and mineral acids [1]. Among other photocatalyst, the well-known TiO_2 material exhibits excellent activity and stability, but requires UV light (only 4% of the solar spectrum) for effective photocatalysis, limiting its practical utility. To overcome this drawback, different approaches such as phase/morphological control, doping, surface sensitization, noble-metal loading, and use of composite materials can be used [2,3]. Examples include photocatalytic oxygen evolution by carbon-coated TiO_2 hierarchical nanotubes [4] and photocatalytic ability of g-C_3N_4 for hydrogen production by Ti_3C_2 MXene Quantum Dots [5]. Also, highly efficient Mn_2O_3 catalysts derived from Mn-MOFs for toluene and CO oxidation [6] as well as toluene oxidation on CuCeZr catalysts derived from UiO-66 metal organic frameworks have been efficiently obtained [7].

Recently, many works on the PC activity of silver-based materials have been reported due to their excellent light sensitivity. However, the performance of these materials is often degraded by particle aggregation and low photostability [8]. Silver chromate (Ag_2CrO_4 - ACO) has emerged as a novel narrow band-gap semiconductor (E_{gap} = 1.80 eV) that is a highly efficient visible-light-driven photocatalyst due to its unique crystal and electronic structure. Additionally, the relatively large values of both the Ag–O bond length and the O–Ag–O bond angle of the AgO_6 octahedron, that is a constituent cluster of the ACO lattice, enable easier migration of the photogenerated electrons and holes [9]. The PC performance of ACO has been studied and different approaches such as the use of heterojunctions, decoration, organic frameworks, composites and aggregates have been investigated for its improvement [9–14]. Some examples include the Z-scheme g-C_3N_4/ACO for hydrogen generation [8], ZnO/ACO nanocomposites with n-n heterojunctions [11], In_2O_3/ACO composites [9], and ACO/SnS_2 [12], among others [15,16]. Electrochemical properties of ACO [17] and its electrical conductivity in different media [18,19] have also been studied. Crystallization and dissolution of ACO [20,21], and the influence

of the $CrO_4^{2-}/Cr_2O_7^{2-}$ template in the formation of a series of silver-chalcogenide clusters [22] were also examined.

Moreover, due to the increased prevalence of diseases and drug-resistant bacteria, the synthesis of new materials for bactericidal and fungicidal application is vital. Silver-containing composites can be exploited as promising candidates for this purpose and have also attracted attention due to their surface plasmon resonance effect [23–25]. In previous studies, our research group has successfully used Ag_2WO_4 [26–32], Ag_2MoO_4 [31], and $AgVO_3$ [33] as potent bactericidal and fungicidal agents.

ACO was obtained and studied in different conditions [34] and the growth of silver nanoparticles induced by electron irradiation [35] was examined. In addition, laser- and electron-beam-induced formation of the Ag-Cr structures on the Ag_2CrO_4 [36] and Zn:Ag_2WO_4 materials [37] has already been studied. These materials showed high performance for biological and catalysis applications. However, to the best of our knowledge, studies of the Ag_2CrO_4:Zn solid solutions have been lacking. This joint experimental and theoretical work investigates the effect of the addition of different amounts of Zn into the ACO host lattice on the structural, electronic and optical properties, and on the enhancement of its photocatalytic and bactericidal activities.

Experimental Section

Synthesis

$(Ag_{2-4x}Zn_{2x})CrO_4$microcrystals were prepared by the co-precipitation (CP) method. First, silver nitrate (2.0 mmol, $AgNO_3$ - 99%, Sigma-Aldrich) and potassium chromate dihydrate (1.0 mmol, $K_2CrO_4.2H_2O$ - 99.8%, J.T.Baker) were dissolved separately in deionized water (50 mL) at room temperature under magnetic stirring for 5 min. Then, the two solutions were mixed together and a dark brown suspension was formed instantaneously. The resulting solution was maintained under stirring for 30 min and the crystals were obtained as a fine powder precipitated at the bottom of the glass flask after the stirring was turned off. For the Zn-solid solution samples, zinc nitrate ($Zn(NO_3)_2$ - 99.999%, Sigma-Aldrich) was dissolved in H_2O and stoichiometric amounts were dissolved with the silver solution; the rest of the procedure was the same as mentioned above. Then the samples were naturally cooled to room temperature and the precipitates were separated by centrifugation and washed with deionized water to remove all remaining sodium and nitrate ions. Finally, the crystals were collected and then dried in

an oven at60 °C for 12 h. The obtained samples were denoted as ACO, ACO1Zn, ACO2Zn, and ACO4Zn corresponding to the pure, 1%Zn, 2%Zn,and 4%Zn-Ag_2CrO_4 solid solutions, respectively.

Characterization

All measurements were performed at room temperature. The nanocrystals were structurally characterized by X-ray diffraction (XRD) using a Shimadzu 600 (Japan) diffractometer with Cu Ka radiation (λ = 1.5406 Å) in the 2θ range from 15° to 60° in the normal mode with a scanning rate of 2°/min and from 10° to 100° with a scanning rate of 0.2°/min in the Rietveld mode. The chemical composition of all samples was estimated by means of inductively coupled plasma optical emission spectrometry (ICP OES) using an ICP OES, the model iCAP 7000 (Thermo Fisher Scientific, USA). The measurements of the elements were carried out using Argon gas (99.996%, White Martins-Praxair, Sertãozinho, SP, Brazil). Fourier-transform Raman spectroscopy (FT-Raman) analysis was conducted using a Bruker RFS/100/S spectrophotometer with a Nd:YAG laser operating at 1064 nm with a maximum power of 60 mW. The shapes and sizes of these nanocrystals were observed using field emission scanning electron microscopy (FE-SEM, Inspect F50, FEI Company, Hillsboro, USA) conducted at 5 kV. Transmission electron microscopy (TEM) and Energy dispersive X-ray spectroscopy (EDS) analysis was performed using a Jeol JEM-2100F with a field-emission gun (FEG) operating at 200 kV. Ultraviolet-visible diffuse reflectance spectra (UV-vis DRS) were obtained using a Cary 5G spectrophotometer (Varian, USA) in the diffuse-reflectance mode. Photoluminescence (PL) measurements were performed at room temperature with the samples excited by a 355 nm laser (Cobolt/Zouk) focused on a 20 μm spot. The backscattered luminescence was dispersed by a 20 cm spectrometer with the signal detected by a charged coupled device detector (Andor technologies).X-ray photoelectron spectroscopy (XPS) was performed using a Scienta Omicron ESCA+ spectrometer with a high-performance hemispheric analyzer (EA 125) with monochromatic Al Kα (hν = 1486.6 eV) radiation as the excitation source. The operating pressure in the ultrahigh vacuum chamber (UHV) during the analysis was 2×10^{-9} mbar. Energy steps of 50 and 20 eV were used for the survey and high-resolution spectra, respectively.

Photocatalysis Procedure

PC activity was tested for the ACO and ACOZn samples for discoloration of rhodamine B (RhB) under visible light irradiation. Each catalyst (ACO, ACO1Zn, ACO2Zn and

ACO4Zn, 50 mg) and RhB solution (50 mL, 10 mg L-1) were used for the tests. The catalyst and RhB solution were added to a beaker and treated by ultrasound (Branson, model 1510; frequency 42 kHz) for 15 min and then stirred for further 30 min for better absorption-adsorption equilibration process. An aliquot was taken at time 0 and the solution was placed under 6-lamp irradiation (Philips TL-D, 15 W), and the system was kept under stirring at a controlled temperature of 20 °C. Subsequent aliquots were collected at specified intervals and centrifuged to remove dust from the catalyst. Dye discoloration was monitored by measuring the RhB absorbance peak (λ max = 554 nm) using a UV-vis spectrophotometer (V-660, JASCO). A control experiment was performed under the same conditions, but without a photocatalyst. To understand the mechanism of the PC process, an experiment using reactive species scavengers was performed by adding 0.1; 1×10^{-3}; and 1×10^{-3} M terbutyl alcohol (TBA), ammonium oxalate (AO), and benzoquinone (BQ), respectively, as the hydroxyl radical (OH*), hole (h•), and superoxide (O_2') radical scavengers, respectively.

Bactericidal and Fungicidal Procedure

The as-synthesized ACO and ACOZn samples were tested to verify their antifungal and antibacterial ability against *Candida albicans* (*C. albicans*) and methicillin-resistant *Staphylococcus aureus* (MRSA). The tests were performed according to the methodology described by Foggi et al.[27,28]. The stock cultures were kept in freeze-dried form at -80 °C. Before the experiments, MRSA was first cultured in onto Mueller Hinton Agar plates (Acumedia Manufactures Inc., Baltimore, MD, USA), while *C. albicans* was streaked onto Sabouraud dextrose agar supplemented with chloramphenicol (0.05 g/L, SDA, Acumedia Manufacturers Inc., Baltimore, MD, USA). After incubation at 37 °C (24-48 h), one loopful of fresh cells of each microorganism grown on the agar plates was transferred to Tryptic Soy Broth (TSB, Acumedia Manufactures, Inc. Baltimore, Maryland, USA) for MRSA, and RPMI-1640 culture medium (Sigma-Aldrich, St. Louis, MO, USA) for *C. albicans*. The cells were incubated overnight (75 rpm; 37 °C), and were then harvested and washed twice with phosphate-buffered saline solution (PBS, pH 7.2) at 5.000 ×*g* for 5 min. Washed bacterial cells were resuspended in TSB for MRSA, while the fungal cells were resuspended in RPMI-1640 culture medium. The suspensions were spectrophotometrically standardized to a final concentration of 10^7 CFU/mL by adjusting the optical density of the suspensions. For viability analysis, the suspensions of each microorganism were incubated with each one of the microcrystals evaluated in 48-well microtiter plates at 37 °C for 48 h. The microcrystals were diluted in the respective liquid media and tested at various concentrations (from 1,000 µg/mL to 0.061 µg/mL). Control

wells were inoculated culture medium without the microcrystal solutions. For the contents of each well, 10-fold dilutions were prepared, and 10 µL aliquots of these were inoculated in duplicate on Mueller Hinton Agar for MRSA and SDA plates for *C. albicans*. The plates were incubated for 24-48 h at 37 °C. After the tests, colony forming units per mL (CFU/mL) were determined and $\log_{10}$ transformed. The assays were performed in triplicate in three independent experiments.

Theoretical Methods and Models Systems

First-principles density functional theory calculations were performed using the CRYSTAL17 program [38,39]. The calculations were performed at the Perdew–Burke–Ernzerh of (PBE) level [40]. All-electron extended by Ruiz [41], 86-411d41G [42], and 6-2111d1G[43] basis sets were used to describe the Ag, Cr, and O atoms, respectively. Additionally for Zn atoms, a pob-TZVP [44] all-electron basis set was used. All basis sets used in this work were obtained from the CRYSTAL basis set database. The thresholds for the evaluation of the Coulomb and exchange integrals are set to 8,8,8,8, and 16. The shrinking factor is set to 8 for the bulk (28 atoms per cell) and to 2 for the 2×2×2 supercell (224 atoms per cell) calculations of the orthorhombic *Pnma* ACO.

The band structure and density of states (DOS) of the models were constructed along the appropriate high-symmetry directions of the corresponding irreducible Brillouin zone. In this work, we have constructed a 2×2×2 supercell to simulate ACOZn (3.22%) where two Zn^{2+} cation were substituted for two Ag^{+} cations, and simultaneously an Ag^{+} vacancy was generated in the vicinity of the Zn^{2+} cation in order to obtain a neutral unit cell. The energy of formation (ΔE_f) of ACO and ACOZn (3.22%) was calculated as [45,46]:

$$\Delta E_f = \frac{E_f - (wE_{Ag} + xE_{Cr} + yE_O + zE_{Zn})}{NxV} \qquad (1)$$

where E_f is the total energy of the system, E_{Ag}, E_{Cr}, E_O, and E_{Zn} are the energies of the Ag, Cr, O, and Zn atoms, the coefficients w, x, y, and z are the amounts of the Ag, Cr, O, and Zn atoms in the cell, respectively, $N = (w + x + y + z)$ is the total number of the atoms in the system and V is the volume of the system. The calculated values of the formation energy per unit volume for each system are presented in Table SI-1. A negative value of ΔE_f corresponds to a structurally stable ground state. The undoped (pure) system had more negative ΔE_f and thus shows greater stability than the doped systems.

The orthorhombic unit cell (*Pnma*) of ACO has a structure with two types of Ag cation coordination clusters namely [AgO_6](Ag_1) and [AgO_4](Ag_2) as shown in Fig. 1, and Zncations can be substituted at any of these sites. Therefore, to carry out a theoretical study of the electronic properties of the ACOZn systems, we have followed a methodology similar to that described in reference [37], generating two model systems: the first in which the substitution of Zn^{2+} is realized at the Ag_1site,and the second model in which the substitution is realized at theAg_2 site, generating one Ag vacancy. The study of these models will allow us to determine theoretically the effect of the substitution in the Ag_1 *or* Ag_2 sites and then to complement and compared with experimental results.

The cell parameters were optimized and the unit cell was represented using a conventional 2×2×2 cell for the ACO and ACOZn systems ($Ag_1$and Ag_2). Different position for the creation of the Ag vacancy were explored and the most energetically favorable model systems of ACOZn (3.22%) are depicted in Fig. SI6. The more negative values of ΔE_f for the ACOZn model with the substitutions at the Ag_1positions sites revealed that this system is more stable than the system with substitution at the Ag_2 positions site (see Table SI-1).

Results and Discussion

XRD

Fig. 1 illustrates the XRD patterns of the samples prepared by the CP method. It is observed that all of the diffraction peaks are narrow and sharp, indicating that all of the samples are highly crystalline. All samples show diffraction peaks in good agreement with the orthorhombic structure with the *Pnma* (62) space group corresponding to the *CIF* no. 16298 file in the inorganic crystal structure database *(ICSD)*. Thus, no impurities were detected up to the detection limit of the X-ray diffraction equipment, and the percentage of the Zn^{2+}cations was not sufficient to give rise to long-range structural disorder in the samples and to form secondary phases. [8,9,12,47]

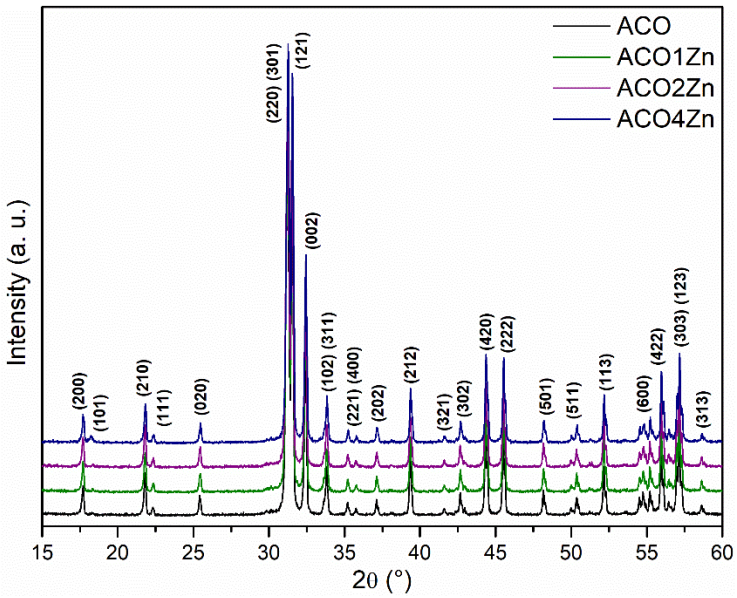

Fig.1. XRD patterns of the ACO and ACOZn samples in the 2θ range of 15-60°.

Rietveld analysis of the prepared samples was carried out to determine the structural properties of the orthorhombic ACOZn samples. Refinement calculations were performed using the TOPAS Academic (v.5) software [48].The parameters refined were the scale factor, background, sample shift, crystal lattice, peak broadening, preferential orientation, atomic position, and isotropic thermal parameters. The peak profile was modeled by the fundamental parameters approach[49] and strain-size broadening was modelled using the double-Voigt method [50].

Rietveld refinement plots for the observed pattern versus the calculated pattern of the ACOZn samples are shown in Figs. SI-1 (a-e). The diffraction peaks of all samples were adjusted according to *CIF*.no. 16298 file. Detailed information about the variations of the lattice, crystallite size, site occupancy, and statistical parameters is provided in Table 1.

Table 1. Lattice parameters, unit cell volume and statistical quality parameters obtained by Rietveld refinement of ACO and ACOZn XRD.

Refined formula $(Ag_{2-4x}Zn_{2x})CrO_4$	**Lattice parameters (Å)**			**Cell volume** ($Å^3$)	**Crystalline size** (nm)	R_{Bragg} (%)	R_{wp} (%)	R_{exp} (%)	R_p (%)	χ^2 (%)
	a	**b**	**c**							
x = 0	10.0604	7.0200	5.5363	391.002(0.01)	86.957	1.37	6.48	3.49	4.78	1.85
x = 0.02	10.0603	7.0201	5.5363	391.006(0.06)	94.557	1.35	6.52	3.59	4.94	1.81
x = 0.04	10.0597	7.0199	5.5361	390.956(0.06)	103.288	1.60	6.34	3.53	4.84	1.79
x = 0.08	10.0606	7.0205	5.5365	391.056(0.06)	83.611	1.75	6.87	3.58	5.33	1.91
ICSD no. 16298	10.063	7.029	5.540	391.86	-	-	-	-	-	-
Site Occupancy										
site	0		0.02		0.04		0.08			
Ag1/Zn1	1/0		0.98105(9)/0.009475(5)		0.96897(4)/0.015515(2)		0.92132(5)/0.03934(5)			
Ag2/Zn2	1/0		0.97895(9)/0.010525(5)		0.95103(4)/0.024485(2)		0.91868(5)/0.04066(5)			
Refined composition	Ag_2CrO_4		$(Ag_{1.960(3)}Zn_{0.020(1)})CrO_4$		$(Ag_{1.920(3)}Zn_{0.040(1)})CrO_4$		$(Ag_{1.840(4)}Zn_{0.080(2)})CrO_4$			

The statistical indices (χ^2, R_{wp}, R_{exp}, R_{wp}, R_p) of the refinement indicate that the refinement is converged and achieved highquality [51].The value of R_{Bragg} indicates the structural quality of the prepared sample through the comparison of the observed and calculated hkl reflection intensities [51]. The R_{Bragg} values corroborate the parameters presented in this calculation, confirming that all of the samples were crystallized in an orthorhombic structure with the *Hermann-Mauguin* (*Pnma*) symmetry space group and four molecular formulas per unit cell (Z = 4). The variation observed in the experimental lattice parameters is correlated with occupation of the Ag^+ positions by Zn^{2+} ions.

Fig. 2 shows the unit cell representation of the structure simulated using the visualization for electronic and structural analysis (VESTA) program [52,53] using the lattice parameters and atomic positions listed in Table 1. The system is constituted by elongated $[AgO_6]$ octahedra, distorted off-centered $[AgO_4]$ tetrahedra, and distorted $[CrO_4]$ tetrahedra. The Zn cations can be substituted at both $[AgO_4]$ tetrahedral and $[AgO_6]$ octahedral Ag sites.

The refinement results show that the Zn^{2+} cations occupy different sites in the ACO lattice. In the $Ag_{2-4x}Zn_{2x}CrO_4$ ($x = 0.01$ and 0.02) samples, Zn^{2+} cations occupy the Ag_2 sites corresponding to the $[AgO_4]$ cluster. For $Ag_{2-4x}Zn_{2x}CrO_4$ ($x = 0.04$), the substitution occur at this site, and at the Ag_2 site of the $[AgO_6]$ cluster. The $[ZnO_w]$ ($w = 4$ and 6) arrangements are represented by distorted tetrahedral and octahedral clusters,

respectively. The occupations of the Zn^{2+} cations lead to distortions in the ACO lattice indicated by the different values of the bond lengths and bond angles. Zinc cations have twice the charge of silver, leading to the rearrangement of the zinc, silver and chromium clusters. Additionally, silver vacancies are formed for charge compensation. With increasing dopant concentration, there is a change in the values of the surface energy, E_{surf}, of the different surfaces, and then a change in the morphology of the crystal is observed. On the other hand, the disturbances of the clusters that form the crystals oscillate, producing variation in the crystallite size. This complex crystal formation structure maintains the principles of randomness, symmetry, and defect optimization. It is also necessary to take into account the different types of the interactions involved that also cause profound changes in crystal growth kinetics. Theoretical models of the samples were built based on the results of Rietveld analysis (Fig. 2).

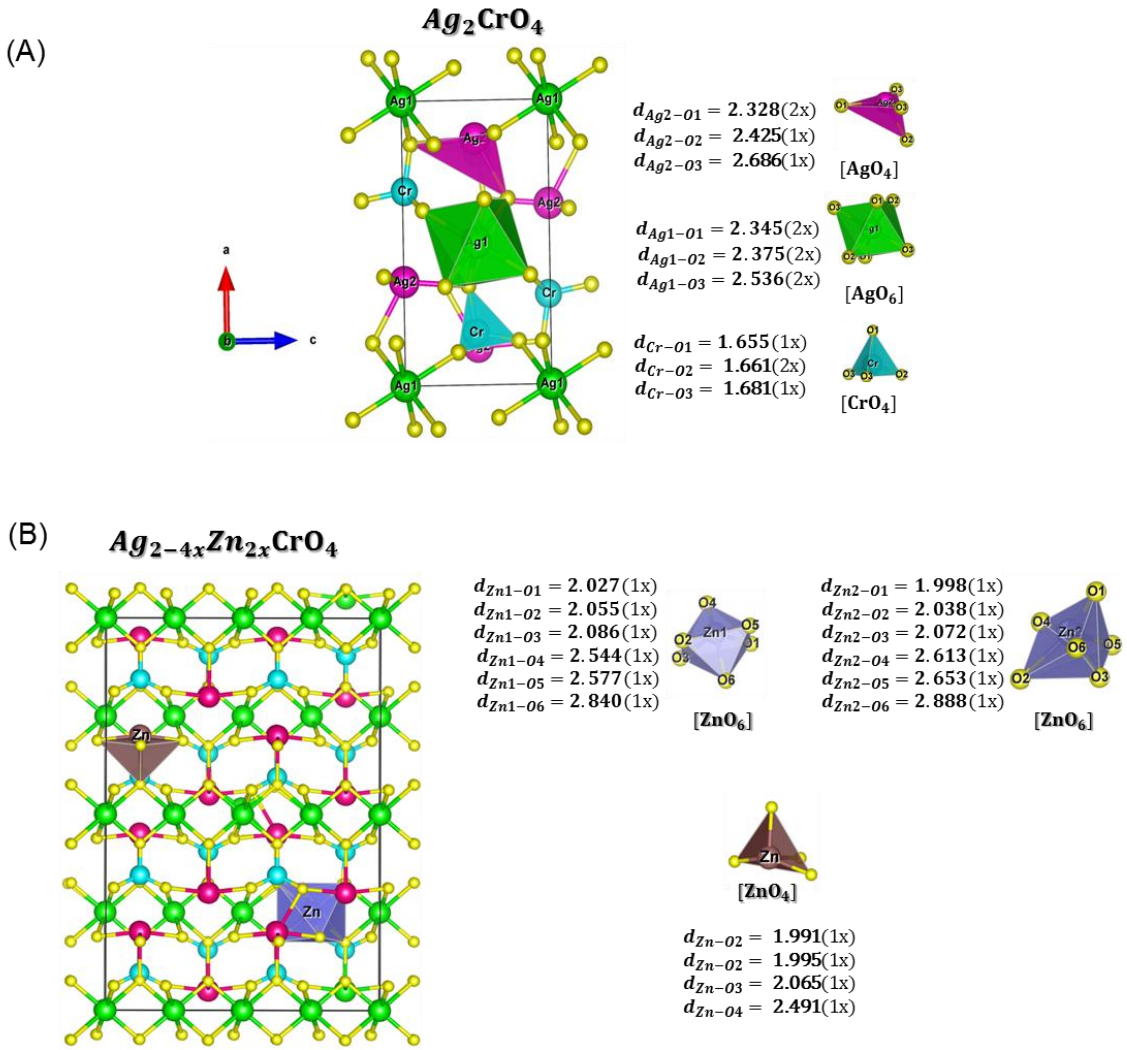

Fig. 2. Schematic representation of ACO (A) showing the local structures for $[AgO_4]$, $[AgO_6]$, and $[CrO_4]$ clusters in pink, green, and cyan, respectively, and the bond lengths (in Å) obtained from DFT calculations. In (B) brown and lilac polyhedrons represent the distorted tetrahedral and octahedral symmetries associated with the $[ZnO_4]$ and$[ZnO_6]$ clusters, respectively, in the substituted $Ag_{2-4x}Zn_{2x}CrO_4$system. 1x, 2x, and 3x indicate the bond multiplicity.

According to Table 1, Zn^{2+} cations preferentially occupy the tetrahedral $[AgO_4]$ sites, but the sample with 1% Zn did not have sufficient Zn content to significantly change the cell volume. However, in this case the observed increase in the crystallite size from ~87 nm to 95 nm indicates the increased diffusion rate of the atoms in the structure, favoring the growth of the crystallite.

ICP OES

ICP OES was used to determine the exact content of the Zn dopant. This technique is very sensitivity and presents an excellent detection capability. ICP OES results in relation to the stoichiometric composition for the empirical Zn content in all samples are summarized in Table 2. The results show that the experimental content increase as the theoretical content increase, besides the experimental results are below the theoretical ones. These deviations are within the expected results, because some loss are expected because of the washing and the limit capability of the host lattice to effectively incorporate the Zn ions. Also, the low concentration of Zn, calibration curve, hygroscopic zinc nitrate as well as the sample digestion may influence on the real content estimated. Some similar results were found in other works [54].

Table 2. ICP OES results for Zn content in ACOZn samples.

Samples	Zn content (mg/L)	
	Theoretical	Experimental
ASO1Zn	3.980	1.53
ASO2Zn	8.031	2.44
ASO4Zn	16.367	5.91

FE-SEM

Figs. 3 (A–D) show the FE-SEM images and size distributions of the ACO and ACOZn microcrystals. Agglomerated particles with different shapes and sizes are observed that can be related to the dissolution, crystallization, and recrystallization processes. [55]

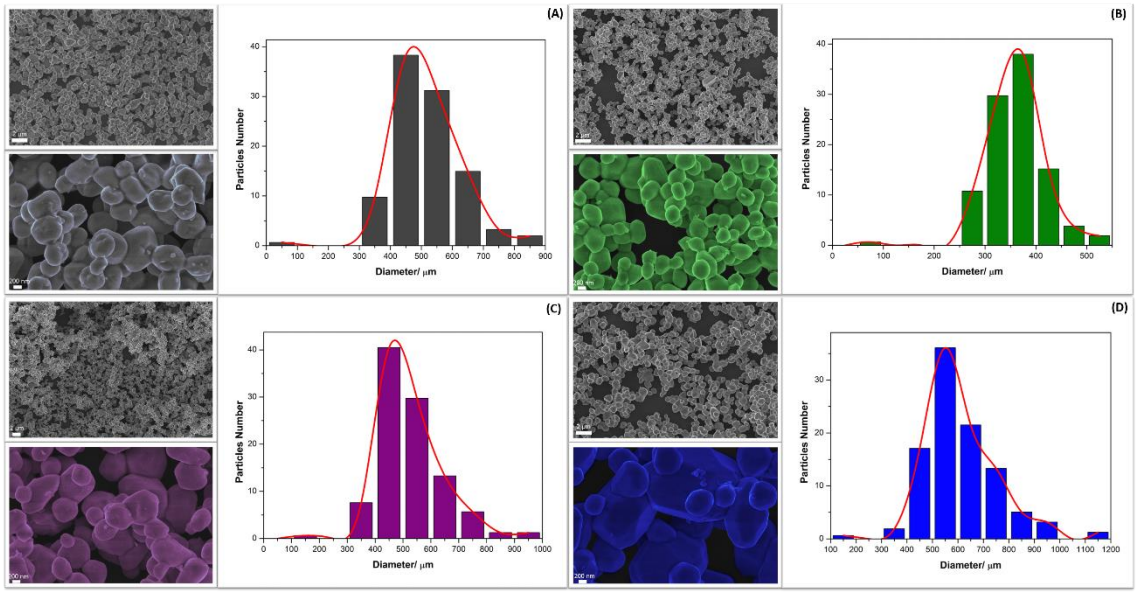

Fig. 3 FE-SEM images and size distributions of (A) ACO, (B) ACO1Zn, (C) ACO2Zn, and (D) ACO4Zn microcrystals obtained by the CP method.

Fig. 3(A) shows the FE-SEM images of the ACO microcrystals with irregular sphere-like morphologies and elongated faceted structures, and undefined morphology. Figs. 3(B–D) show the FE-SEM images of the ACOZn (1, 2, and 4%) microcrystals, respectively. Analysis of these images shows that the replacement of Ag^{+} by Zn^{2+}cations in the ACO structure has a strong effect on the morphology and size of the ACO microcrystals. This is an indication of the successful substitution of Ag^{+} by the Zn^{2+} cations in the host lattice. These ACOZn samples exhibit an elongated well-defined faceted morphology that becomes more defined with increasing Zn^{2+} cation content in the ACO structure. This behavior and morphological pattern are similar to the results obtained in previous related studies [34,35]. The particle size distributions are shown in Figs. 3(A–D), and the analysis of these results indicates that the size of the ACOZn microcrystals increases with the amount of the Zn cations. The average particle sizes of the samples were 476, 365, 470, and 550 nm for ACO, ACO1Zn, ACO2Zn and ACO4Zn, respectively.

The ACO morphologies are composed of the combination of the (001), (010), (100), (011), (110), (101), and (111) surfaces, where each exposed ACO surface is formed by different types of under-coordinated [AgO_x] and [CrO_4] clusters.[34] Computational simulations based on the E_{surf} values of the different surfaces and the Wullf construction were used to obtain the possible morphologies of a given material[56]. In addition, a comparison between theoretical predictions and experimental results as displayed in the

SEM images can be carried out. This procedure has been used successfully by our research group to elucidate the morphologies of the $PbMoO_4$, Ag_2MoO_4, BaMoO4, $CaWO_4$, Ag_3PO_4, and Ag_2CrO_4 materials. [34,57–61]

The equilibrium morphology of ACO was characterized for the (001), (011), and (110) surfaces, among which the (110) and (011) surfaces dominate in the Wulff shape and comprise almost 70% of the total crystal shape area with the contributions of 55.8% and 27.4%, respectively. The Wulff shape corresponding to the ACO1Zn sample was obtained by increasing the E_{surf}value for the (001) surface and by decreasing the E_{surf}values for the (011) and (110) surfaces, while the morphology of the ACO2Zn sample was obtained by increasing the values of the $E_{surf}$of for the (001) and (011) surfaces and decreasing the E_{surf}values for the (100) and (101) surfaces. The ACO4Zn sample was obtained by increasing the E_{surf} values for the (100), (101), and (001) surfaces and by decreasing the E_{surf}value for the (011) surface.

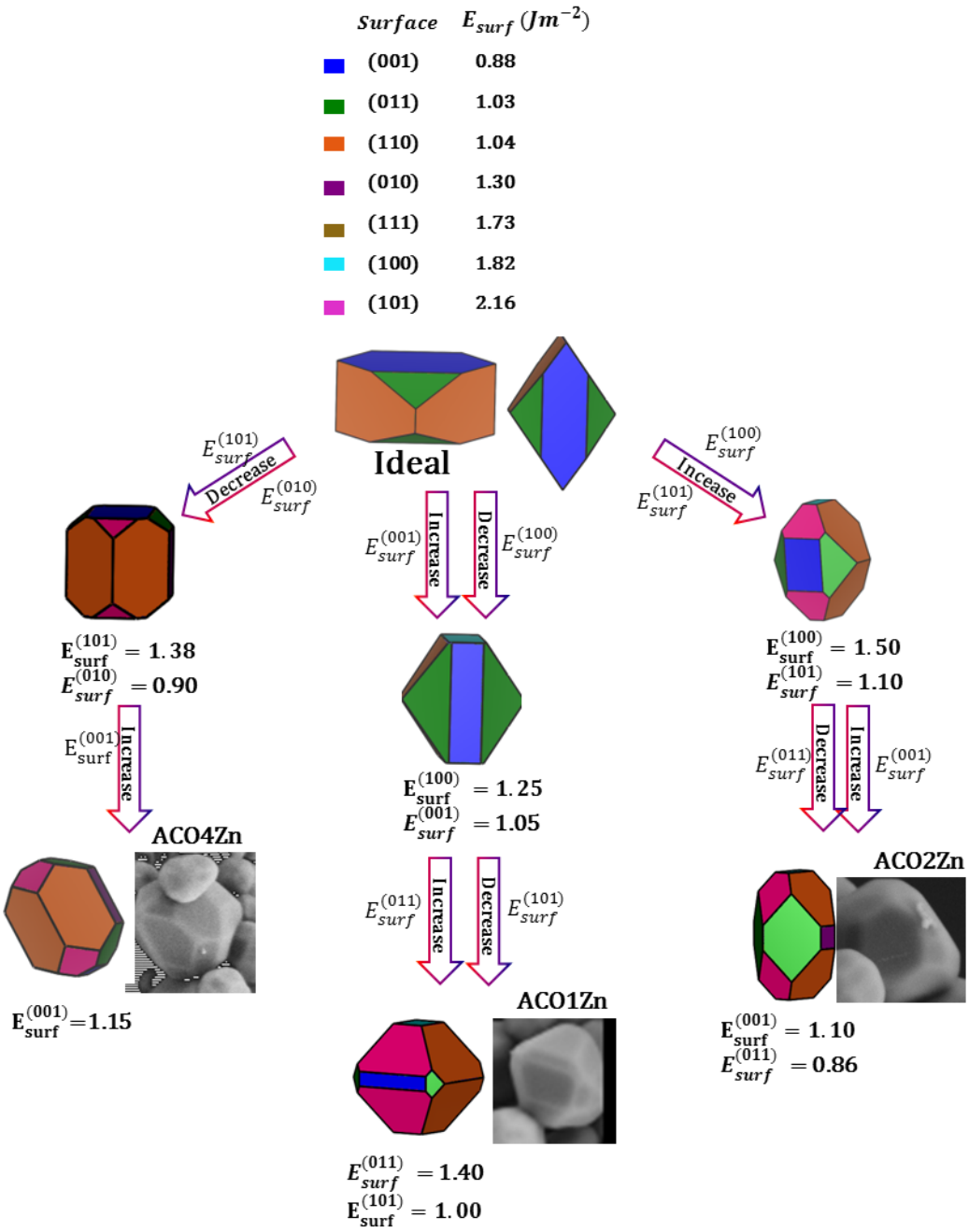

Fig. 4. Wulff construction for ACO. Experimental SEM images are shown in the insets for comparison. E_{surf} values are given in Jm^{-2}.

We also calculated the energy profiles of the paths connecting different morphologies based on the polyhedron energy (E_{pol}) values by using the following expression [62]:

$$E_{pol} = \sum C_i \, x \, E_{surf}^{i} \qquad (2)$$

where C_i is the percentage contribution of the surface area to the total surface area of the polyhedron, $C_i = A^i/A^{polyhedron}$, and E^i_{surf} is the surface energy of the corresponding surface. The energy profiles were calculated by decreasing and/or increasing the E_{surf} values of a given surface of the polyhedron. Fig. 5 displays the energy profile connecting the ideal morphology of ACO with the final experimental morphologies of ACO1Zn, ACO2Zn, and ACO4Zn. The values of E_{pol} calculated using equation 2 for the selected morphologies are summarized in Table SI-2.

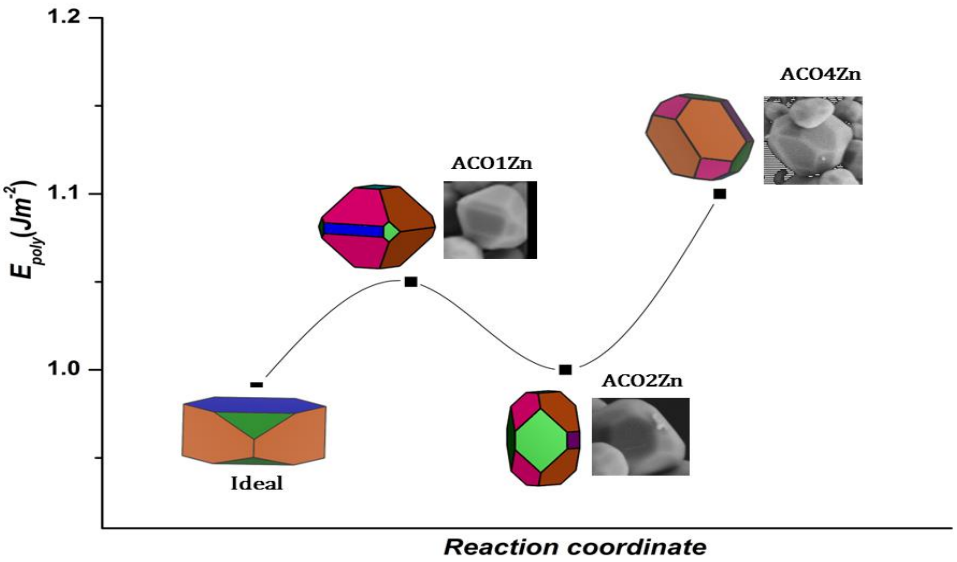

Fig. 5. Energy profile of E_{pol} values vs the reaction coordinate connecting the ideal morphology and different experimental morphologies of ACOZn samples. Experimental morphologies as observed by FE-SEM are presented in the insets for comparison.

The pathway connecting the ideal morphology with those displaying excellent agreement with the experimental ACOZn morphologies is presented in Fig.5. An analysis of the results shows that the pathway from the ideal morphology to the ACO2Zn morphology presents an energetic barrier *via* a maximum that corresponds to the ACO2Zn sample. Starting from this morphology, an important gain in E_{pol} is necessary to reach the ACO4Zn sample. For all substituted samples, the E_{pol} values are higher than the E_{pol} of the pure crystal (*Ideal shape*), indicating that the unsubstituted system is more stable, in accordance with the ΔE_f values reported in Table SI-1 that predict the greater stability of the unsubstituted crystal.

TEM

Transmission electron microscopy (TEM) images of ACO and ACO2Zn samples are shown in Fig. 6(A) and (B), respectively. It is possible to observe faceted-like particles for both samples with a size of approximately 300 nm for ACO and 400 nm for ACO2Zn. The Energy dispersive X-ray spectroscopy (EDS) technique was used to check the elemental compositions and quantity of the ACO and ACO2Zn samples, and the results are shown in Fig. 6(C) and (D), respectively. It can be seen that ACO sample is composed of only Ag, Cr and O elements, and no other element or impurity is found besides C and Cu of the grid. Quantitative analysis of this sample presents an atomic percentage of approximately 37.53% Ag, 19.12% Cr, and 43.33% O. For the ACO2Zn sample, it was also present a peak related to Zn, and this sample presents an atomic percentage of approximately 37.16% Ag, 16.73% Cr, 43.40% O, and 2.69% Zn. The results are in accordance with the theoretical percentages, and small deviations are due to the region of the analysis, also indicating that both structures are pure.

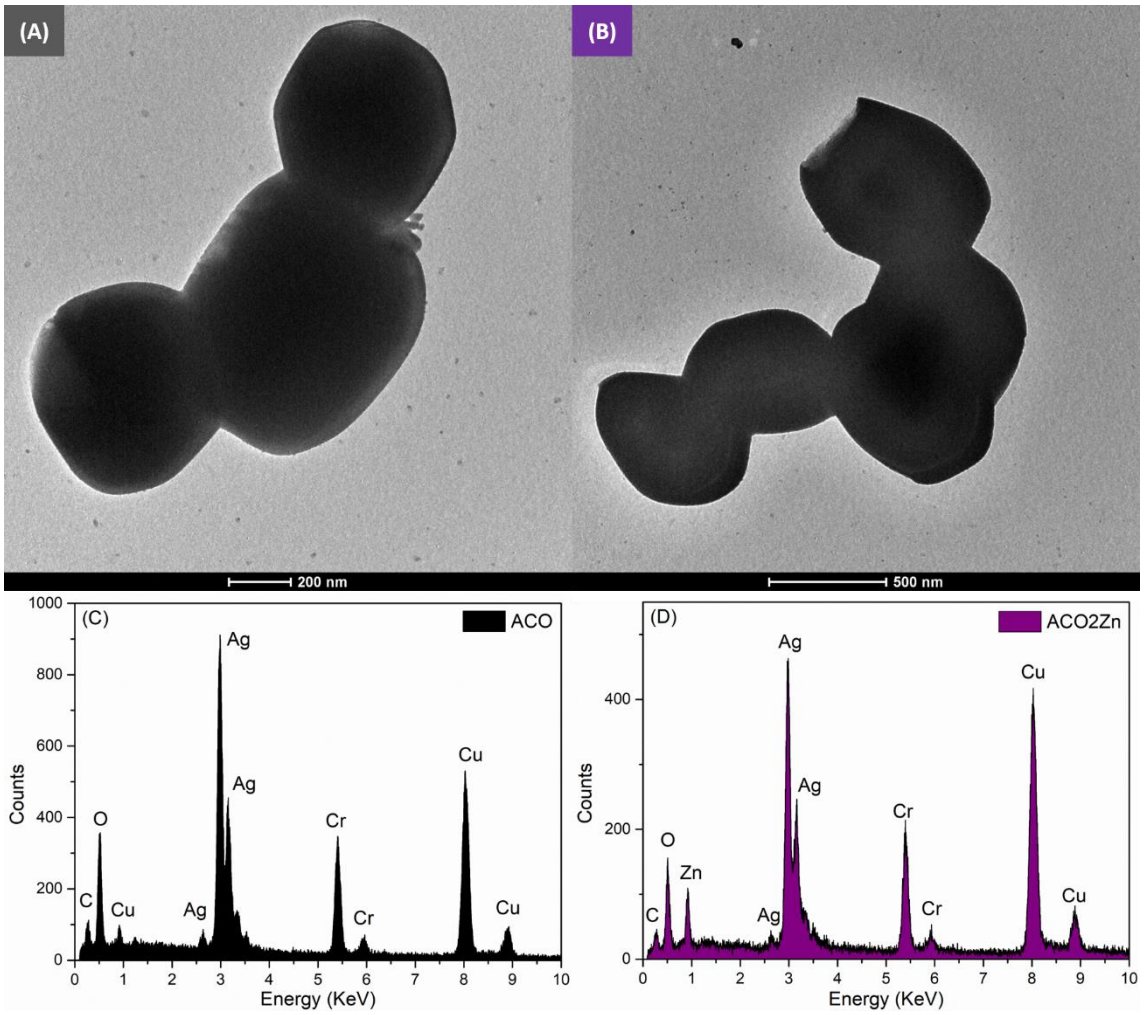

Fig. 6. (A) TEM image and (C) EDS spectra of ACO and (B) TEM image and (D) EDS spectra of ACO2Zn.

XPS

XPS was used to examine the surfaces of the ACOZn samples to provide information such as chemical composition, binding energy, atomic bonding configuration, electronic structure and oxidation state of the constituent atoms. Survey spectra of the samples are presented in Fig.7, where the C, Ag, Cr, and O peaks are clearly observed for all of the samples, and the Zn peak is observed for the ACOZn samples. No other elements due to impurities were identified.

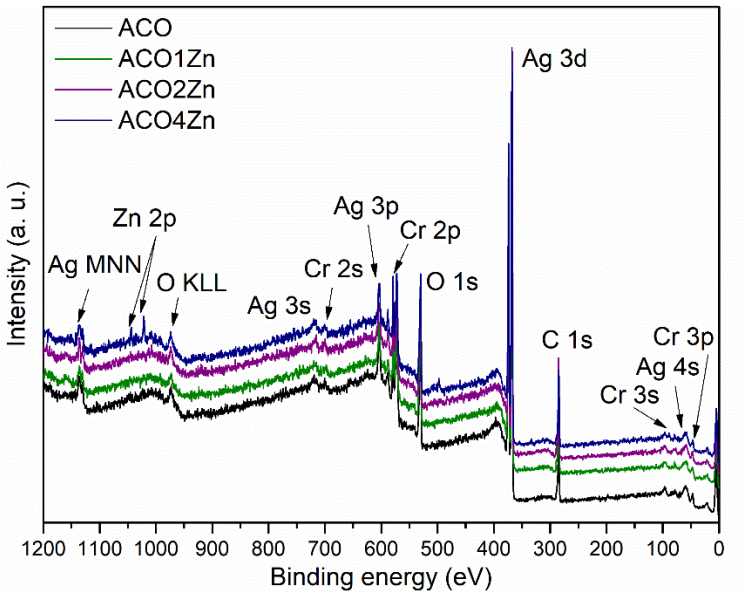

Fig. 7. XPS survey spectra of the ACO and ACOZn samples.

The Ag 3d high-resolution spectrum in the range of 364–380 eV presents two peaks, as shown in Figs. SI-2(a-d). The two deconvoluted components located at 367.5 and 373.5 eV (Δ = 6 eV) are attributed to Ag $3d_{5/2}$ and Ag $3d_{3/2}$, respectively, confirming the presence of the Ag^{+} ion. Another two deconvolution components observed at 368.4 and 374.4 eV(Δ = 6 eV) are due to the presence of Ag^{0} that can be related to the surface coating of Ag nanoparticles on the materials [63–67].

The Cr 2p high-resolution spectrum in the range of 576–592 eV is shown in Figs. SI-3(a-d). Following previous studies, the doublet Cr 2p peak at578.8 eV (Cr $2p_{3/2}$) and 588.1 eV (Cr $2p_{1/2}$) is attributed to Cr^{6+} [9,10,12,13].

The O 1s high-resolution spectrum is shown in Figs. SI-4 (a-d) and exhibits three main components. The components at 529.8 eV and 530.9 eV are attributed to the lattice oxygen and are related to the Ag-O and Cr–O chemical bonding in the ACO. The peak at 532.4 eV can be assigned to the water species or the external -OH groups adsorbed on the surfaces of the materials [68–70].

The high-resolution Zn 2p spectra in the range of 1017–1050 eV are shown in Figs. SI-5 (a-c). The Zn2p peak shows a significant spin-orbit splitting for the components located at 1021.5 and 1044.5 eV (Δ = 23 eV) that can be assigned to Zn $2p_{3/2}$ and Zn $2p_{1/2}$, respectively. These components indicate that the Zn is present in the +2 oxidation state [71–73]. Thus, all of these findings clearly confirm the existence of ACO and Zn ions as well as the purity of the samples.

FT-Raman

ACO crystallizes in the *Pnma* (D_{2h}^{16}) space group with four formula units per unit cell (Z = 4), with the $[CrO_4]^{2-}$ ions occupying the C_s symmetry sites. Its structure exhibits 36 Raman-active modes according to group theory analysis that are expressed by the reductive equation, $\Gamma = 11A_g + 7B_{1g} + 7B_{3g} + 11B_{2g}$. Fig. 8 presents the FT-Raman spectra obtained using 633 nm laser excitation of the ACOZn samples prepared by the CP method. Four modes centered at 338, 352, 358 and 373 cm^{-1} were detected in the medium frequency range and can be assigned to the B_{2g}, A_g, B_{3g} and B_{2g} modes, respectively. These weaker intensity modes are related to the bending modes of the $[CrO_4]$ group. The most intense Raman modes are the stretching modes of the $[CrO_4]$ group in the high-frequency region centered at 776, 811, 826, 846, 856, 860, and 865 cm^{-1} that can be assigned to the B_{2g}, A_g, A_g, B_{3g}, B_{2g}, B_{2g}, and B_{2g} modes, respectively. Low-intensity modes in the low-frequency region (below 150 cm^{-1}) were too weak to be identified. Other modes could not be assigned because in some cases the splitting are too small to be resolved and also due to the presence of some component bands [35,74–76]. These Raman modes confirm the short-range order of the samples and demonstrated that the small amount of Zn ions was not sufficient to give rise to strong structural changes of the host lattice.

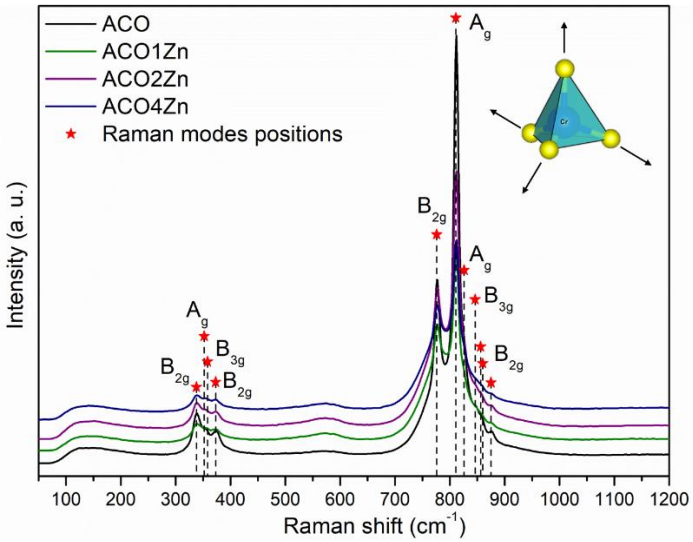

Fig.8. FT-Raman spectra of the ACO and ACOZn samples obtained using a 633 nm laser.

Optical properties

The activation energy of the photocatalyst for the formation of the electron-hole pairs that carry out the reduction and oxidation of molecules is given by the band-gap

energy (E_{gap}). E_{gap} corresponds to the energy required for the transition of electrons from the valence band (VB) to the conduction band (CB) and is generally estimated by UV-vis DRS [77]. Fig.9 (A) shows the UV-vis DRS of the ACOZn samples within the 400–800 nm range. The samples showed absorption in the visible region at about 650 nm, strongly favoring the catalytic efficiency of these materials, because the sensitivity to visible light enables the use of solar radiation for the reaction. The electronic profile of the ACOZn samples is a result of the hybridization of the Ag 4d and O 2p orbitals forming the VB, while the position of the CB is controlled by the antibonding interaction between the Cr 3d and O 2p orbitals. This electronic configuration is responsible for the strong absorption in the visible spectrum. The E_{gap} values were obtained by linear extrapolation of the UV-vis DRS curves in the graph of $[F(R_\infty)hv]^n$ versus hv, that were calculated using the Kubelka-Munk relation and the Wood-Tauc function [78,79]. The $F(R_\infty)$ is the Kubelka-Munk function, hv is the photon energy, and n is the constant related to the type of the electronic transition of a semiconductor, with $n = 0.5$ for direct allowed, $n = 2$ for indirect allowed, $n = 1.5$ for direct forbidden, and $n = 3$ for indirect forbidden. Theoretical calculations show that ACO has an indirect allowed transition [35,80,81], i.e. the VB minimum and the CB maximum are located at the different points of the Brillouin zone. Therefore, for all samples, $n = 2$ was considered in the equation. The obtained E_{gap} values were 1.73, 1.72, 1.68, and 1.75 eV for the ACO, ACO1Zn, ACO2Zn, and ACO4Zn samples, respectively (see Fig. 9(B)). The E_{gap} value of 1.73 eV for the pure ACO is in agreement with the values reported in the literature [8,35,82]. Small deviations were observed for the Zn-solid solutions, as a result of the different energy of the 2p orbital of Zn which contribute in both CB and VB, as predicted theoretically [37].

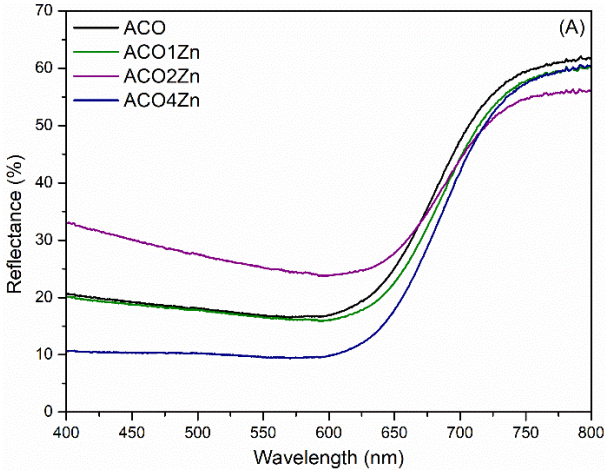

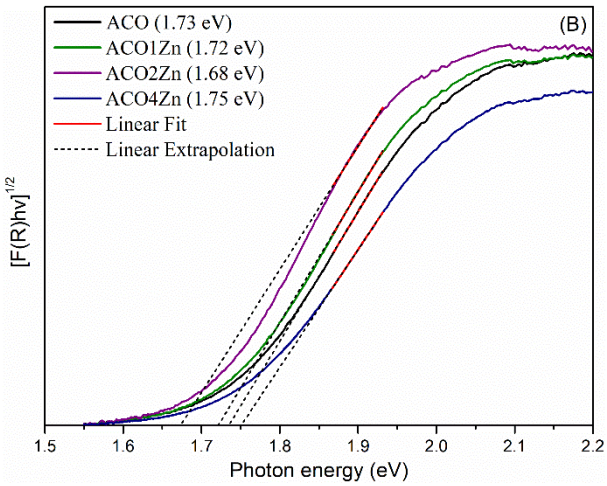

Fig. 9. (A) UV-vis DRS of the ACO and ACOZn samples; (B) Energy gap estimated by the Kubelka-Munk and Wood-Tauc functions.

PL

The PL spectra are useful for rationalizing the processes involving charge separation and transfer and the recombination processes of the photoinduced electron-hole pairs in a semiconductor, which in turn provides information about the PC activity. It is widely believed that a stronger PL intensity indicates a higher recombination rate of the photogenerated charge carriers and conversely, a weaker PL intensity indicates a higher separation probability of the photogenerated charge carriers. Therefore, at higher PL intensity, fewer photoinduced electrons and holes participated in the PC oxidation and reduction reactions, resulting in lower PC activity efficiency. Moreover, a large proportion of electron-hole pairs recombine, dissipating the input energy in the form of heat or emitted light. Fig. 10 shows the PL spectra of the samples under laser excitation at the wavelength of 355 nm.

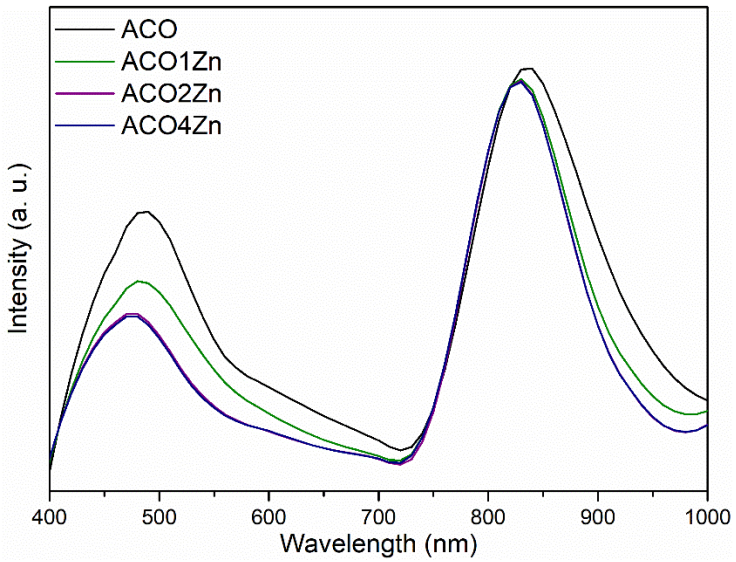

Fig. 10. PL spectra of the ACO and ACOZn samples excited by a 355 nm laser.

ACOZn samples present an intense absorption band centered at approximately 450 nm that is responsible for the red color of the samples. The explanations proposed for the appearance of this absorption band and its possible assignments may be summarized as follows: (1) transfer of an Ag^{+} 4d electron to the lowest unoccupied e orbitals of the $[CrO_4]^{2-}$ anion (an interionic transition); (2) a shift of the $^{1}T_2 \leftarrow {}^{1}A_l$ transition of the $[CrO_4]^{2-}$ ion to a lower energy due to the "second-order Davydov interaction" between the $^{1}T_2$ excited state of the $[CrO_4]^{2-}$ anion and an excited state of the Ag^{+} cation resulting from the 5s ← 4d or 5p ← 4d intraionic transitions; (3) induction of allowed character to the $^{1}T_1 \leftarrow {}^{1}A_1$ ($t_1{}^5e \leftarrow t_1{}^6$) transition (which is very weak, at ~22500 cm^{-1}, for K_2CrO_4) due to the lowering of symmetry of the $[CrO_4]^{2-}$ group in the ACO lattice [74]. Another band centered at 835nm appears for all ACOZn samples as was reported in other studies related to the ACO structure [34]. The higher-energy band is due to the shallow defects that are associated with the order−disorder clusters, and the lower-energy band (red region) is ascribed to the presence of oxygen vacancies.

These results indicate the presence of the medium-range structural and electronic order−disorder characteristics and is characteristic of a multiphonon and multilevel process. It is believed that Zn^{2+}cations are responsible for the creation of new levels within the band gap of the semiconductor, which in turn improves the charge separation process, modifying the PL intensity, and as a consequence also favoring the PC process. Finally, these results are in agreement with the theoretical analysis as discussed in the electronic properties section.

PC Activity

PC tests were performed for the ACO, ACO1Zn, ACO2Zn, and ACO4Zn samples for rhodamine B (RhB) degradation process under visible light irradiation. Testing was also performed under the same experimental conditions and without the presence of catalysts, known as photolysis. Degradation was evaluated by aliquoting at certain reaction times (0, 2, 5, 10, 15, 20, 30, and 40 min) and then measuring the absorption spectrum from 450 to 650 nm by UV-vis spectrophotometry. Discoloration is assessed by the maximum absorption of rhodamine-B at 554 nm. Fig. 11 shows the UV-visible absorption spectra for RhB photodegradation for different photocatalysts, where it is observed that the Zn-containing samples show higher PC activity than the pure ACO sample.

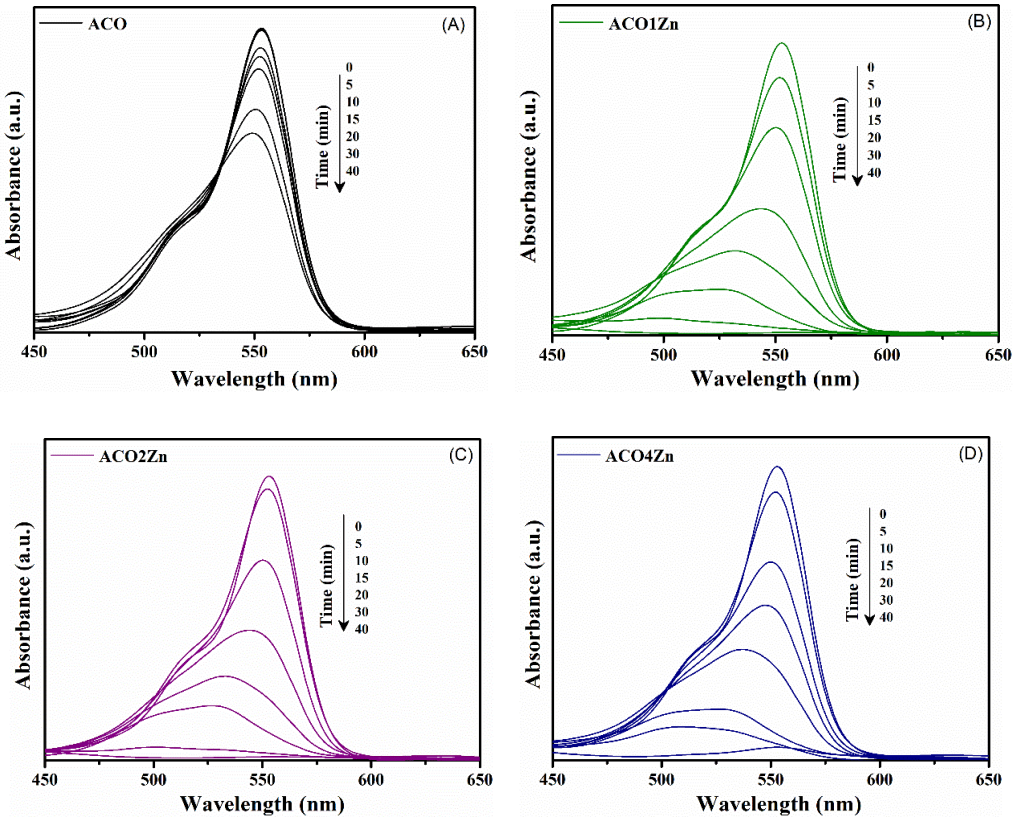

Fig. 11. UV-visible absorption spectra for RhB photodegradation with different photocatalysts; (A) ACO; (B) ACO1Zn; (C) ACO2Zn; and (D) ACO4Zn.

Fig.12(A) shows the variation of RhB absorbance (A_N/A_0) as a function of the irradiation time, where A_0 and A_N are the initial absorbance after the adsorption-desorption equilibrium of the photocatalyst and reaction medium and absorbance at irradiation time t, respectively. RhB photolysis experiment under visible light irradiation

showed no significant discoloration. As discussed above, the ACOZn samples discolored virtually all RhB in approximately 40 min while pure material discolored approximately 40% during the same time period. For better understanding of the data, kinetic analysis was performed using the Langmuir-Hinshelwood model, considering a pseudo first-order function given by [83]:

$$-\ln (A_N / A_0) = k't \qquad (3)$$

where k' is the velocity constant and t is the irradiation time. The results of the analysis are shown in Fig.12(B). The ACO1Zn and ACO2Zn samples showed very close k' values that were higher than those of the other samples. The ACO sample had k'= 0.0118 min^{-1} and the ACO2Zn sample had k' = 0.117 min^{-1}, demonstrating that the addition of Zn leads to an order of magnitude improvement in the PC activity of ACO. Zhu et al.[84] obtained k' of 0.06 min^{-1} for RhB degradation using the $AgBr/Ag_2CrO_4$ compound. In another study, Deng et al.[85] developed the $Ag_2CrO_4/g\text{-}C_3N_4$ material and its PC activity was evaluated for RhB degradation, obtaining k' = 0.09 min^{-1}. These values are lower than the value reported in the present study, demonstrating the effectiveness of the use of Zn^{2+} ions for improving the PC activity of ACO samples. On the other hand, analysis of the k' values also shows that the k' of the ACO4Zn sample is significantly lower than those of the other ACOZn samples; this may be related to the occupation of the interstitial and surface sites of the host lattice instead of the Ag sites, decreasing k'. The PC efficiency of the pure sample is strongly decreased by the high recombination rate of the photogenerated electron-hole pairs, giving rise to very poor response to visible light as well as the possibility of photocorrosion.

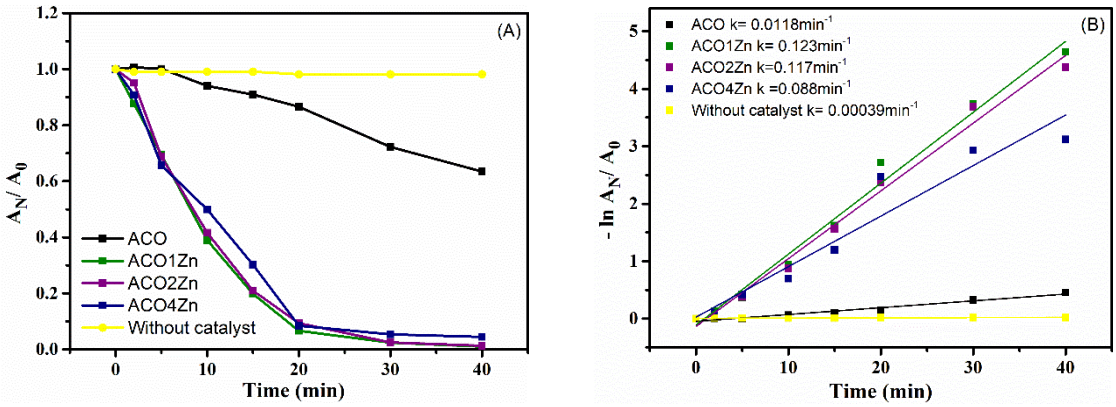

Fig. 12. (A) PC degradation of RhB in the absence and presence of the catalyst shown in a linear plot and (B) in a log-scale plot for the determination of the rate constant using the Langmuir-Hinshelwood model.

Due to the observed improvement in the PC efficiency of the ACOZn samples, experiments using reactive species scavengers were performed in order to understand the reaction mechanism. As shown in Fig. 13, PC experiments using BQ and AO showed a sharp decrease in rhodamine-B discoloration. This indicates that O_2' and h• play the main role in the discoloration mechanism of rhodamine-B using the ACOZn samples as photocatalyst. The structure of ACO is composed by octahedral [AgO_6] and tetrahedral [AgO_4] clusters. The replacement of these Ag^+ by Zn^{2+} cations induces the formation of [ZnO_6]$^\bullet$ and [ZnO_4]$^\bullet$clusters with partially positive charges due to the higher oxidation state of the Zn^{2+} cation relative to the host Ag^+ cation. Thus, because polarization of the local structure, electronic density is generated, forming clusters with partially positive and negative charges in equivalent proportions because the introduction of Zn^{2+} cations lead to the formation of [ZnO_y]$^\bullet$ clusters and Ag vacancies (V_{Ag}'). These residual charge clusters play the main role in the oxidation and reduction processes of the Rhodamine-B PC discoloration mechanism because partially positive charge clusters act as oxidant clusters and silver vacancy acts as reducing species.

Therefore, [ZnO_y]$^\bullet$ clusters are associated with h•, act as oxidants of species such as H_2O with the formation of OH* and H$^\bullet$. V_{Ag}' reacts with the molecular O_2 to produce the O_2' radical. As a result, the introduction of Zn^{2+} cations in the ACO structure induces the formation of oxidizing and reducing clusters, giving rise to increased PC activity of the material. Based on the above considerations, a PC mechanism was proposed as follows:

$[AgO_y] + Zn^{\bullet\bullet} \rightarrow [ZnO_y]^{\bullet} + V_{Ag}^{'}$ where y = 4 or 6 [1]

$[ZnO_y]^{\bullet} + H_2O \rightarrow OH^* + H^{\bullet}$ [2]

$V_{Ag}^{'} + O_2 \rightarrow V_{Ag}^{x} + O_2^{'}$ [3]

$O_2^{'} + H^{\bullet} \rightarrow O_2H^*$ [4]

$RhB + O_2H^* \rightarrow$ degradation products + H_2O, [5]

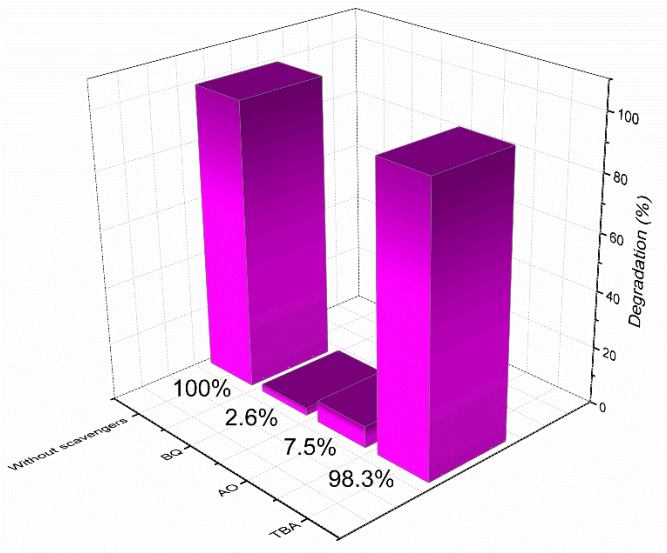

Fig. 13. Influence of various scavengers in the PC degradation of RhB in the presence of the ACO2Zn catalyst.

In order to evaluate the stability of the proposed materials, stability cycles of the ACO and ACO2Zn samples were performed, the latter with the best photocatalytic result. To perform this experiment, the same powder from each material was reused 3 times, being the powder washed with deionized water and centrifuged after each run cycle. The results are shown in Fig. 14, where it is possible to observe that the ACO sample decreases its photocatalytic activity at each cycle, discoloring only 20% of the dye in the third photocatalytic cycle, thus demonstrating that the material does not have stability. In contrast, the ACO2Zn sample discolored the RhB dye in a shorter time and also proves to has greater stability than the pure material. Even after 3 running cycles, the ACO2Zn sample degrades 90% of the dye. Thus, Zn substituted Ag_2CrO_4 showed an improvement of the photocatalytic activity of the material and its greater stability. The XRD patterns

of the ACO and ACO2Zn after the stability cycles are shown in Fig. SI-6. It was observed all diffraction peaks are related to the orthorhombic structure with the *Pnma* (62) space group. However, after the cycles, the samples are less crystalline, probably because of dye adsorption and light exposure which contribute to decrease the long-range order of the samples. The ACO sample present lower crystallinity after the cycles than ACO2Zn sample, confirming the stability and greater performance for PC applications of the ACO2Zn sample. [3]

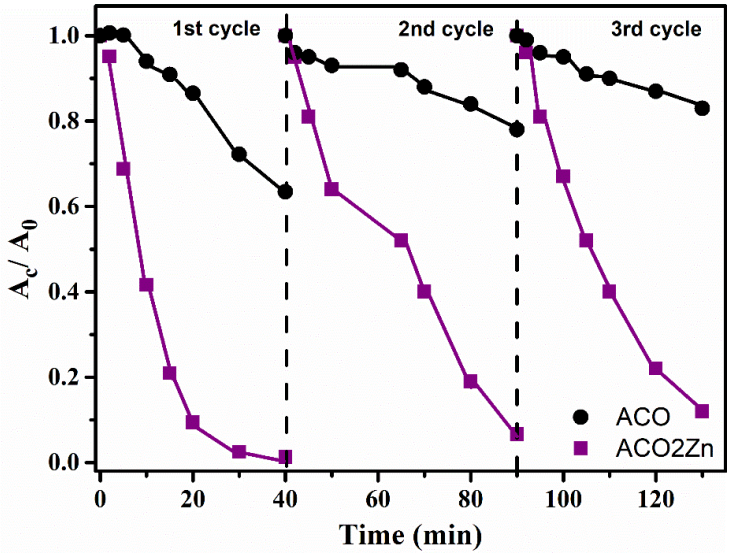

Fig. 14. Cycling runs for RhB photodegradation over ACO and ACO2Zn samples under visible light irradiation.

On the basis of the aforementioned results, a schematic mechanism was proposed to explain the photocatalytic properties of the ACO2Zn sample. The degradation of dyes using photoactive materials in an aqueous solution depends mainly on the band gap, surface area, amount of the catalyst, and generation of an electron−hole ($e^-h\cdot$) pair. The semiconductor´s activation is realized through the absorption of a photon of ultra-band gap energy, which results in the promotion of an electron e^- from the VB to the CB, with the concomitant generation of a hole ($h\cdot$) in the VB. The photocatalyst is efficient, if the major deactivation processes involving e^--$h\cdot$ recombination is low [3]. It was discussed that besides the recombination process that always occurs, Zn plays an important role to avoid this mechanism, contributing to higher photocatalytic activity of ACO2Zn sample. For ACO sample, the photogenerated electron-hole pairs quickly recombined and only a fraction of them participated in the PC reactions. The schematic diagram of the

photogenerated electron–hole pairs transfer pathway of the ACO2Zn under visible light irradiation is shown in Fig. 15.

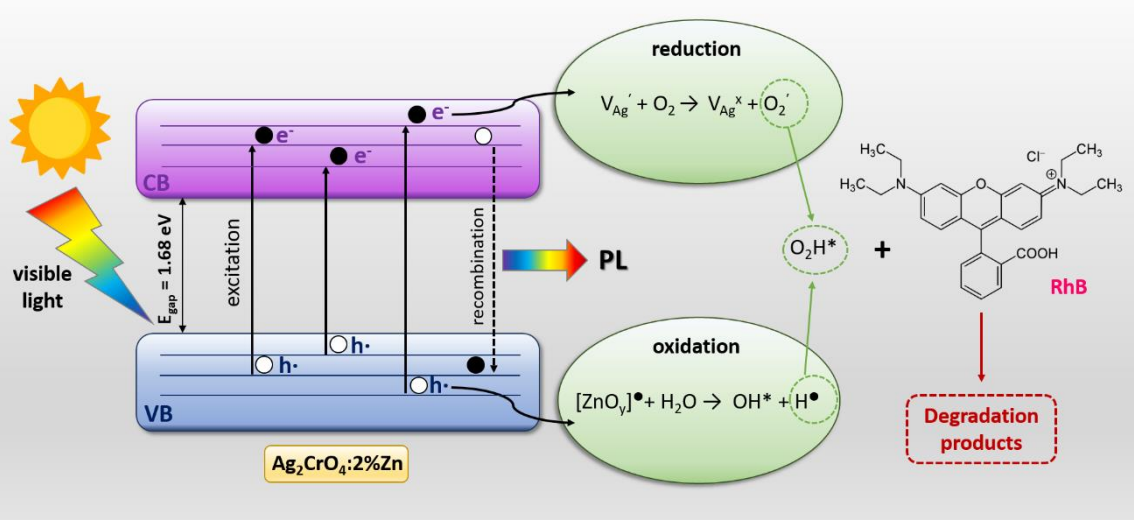

Fig. 15. Schematic diagram of the photogenerated electron–hole pairs transfer pathway of the ACOZn under visible light irradiation.

Electronic properties

The structure of the orthorhombic ACO unit cell (*Pnma*) contains two types of coordination clusters for the Ag^+ cation, namely [AgO_6] (Ag_1) and [AgO_4] (Ag_2) as shown in Fig. 2, and the substitution of Zn^{2+} cations can occur at any of these sites, depending on the concentration of Zn^{2+} cations. Therefore, to carry out a theoretical study of the electronic properties of ACOZn systems, we have followed a methodology similar to that used in reference [37], and used two model systems: in the first, the Zn^{2+} cation are substituted at the Ag_1 site, and in the second the Zn^{2+} cations are substituted at the Ag_2 sites, generating one Ag vacancy far away from the Zn^{2+} cations.

An optimization of the cell parameters was performed and the unit cell was modeled using a conventional 2 × 2 × 2 cell for the ACO and ACOZn systems (Ag_1 and Ag_2). A schematic representation of the two models of ACOZn (3.22%) showing the Zn^{2+} additions and the Ag vacancy positions is presented in Fig. SI-7. The more negative values of ΔE_f for the ACOZn model with substitutions at the Ag_1 positions revealed that this structure is more stable compared to the system with substitution at the Ag_2 positions (see Table SI-1).

The electronic structure of both pure and ACOZn systems was analyzed in terms of band structure and density of states for 100 k-points along the appropriate high symmetry paths as in reference [34] and the obtained results are shown in Figs. 16-18.

The results revealed that ACO and ACOZn systems have indirect band gaps, which is in agreement with reports in the literature for the ACO structure [8,35,82]. The band-gap transition for ACO is between the Γ and T points in the Brillouin zone, the lowest CB in pure ACO split into three sub-bands along the T point, while for ACOZn, the Zn atoms break the degeneracy, generating flat bands and change across-band-gap transition from Γ-T to Γ-Y and shifting the band gap towards lower energy (Fig.16B and C). For the top VB, degeneracy was not observed in any of the models. The theoretical calculations predict an indirect band gap value of 1.46 eV for pure ACO, which is in agreement with theoretical values reported in the literature [34,80,86,87]

For the ACOZn samples, the experimental Egap values were close to 1.72 and 1.68 eV and the theoretical model ACOZn (3.22%) calculations predict a band-gap of 1.15 eV for the substitution of Zn^{2+} cations at the Ag_1 site (Fig. 16B) and 0.82 eV for the substitution at the Ag_2 site (Fig. 16C), confirming the substitution of Zn^{2+} in the Ag^{+} sites and the formation of new $[ZnO_{y=4,6}]$ clusters in the Ag_2CrO_4 lattice, which affects the band gap. When the substitution occurs in Ag_2 sites, under-coordination $[ZnO_4]$ clusters are generated as well as oxygen vacancies, creating more disorder in the structure and changes in the electronic properties of material due to the rearrangement of the oxygen around the Zn^{2+} cations [37]. On the other hand, $[ZnO_6]$ clusters generated by substitution in Ag_1 sites affect in less scale the electronic properties of the material. In Fig. 17 the band structure alignments for ACO, ACOZn (Ag_1) and ACOZn (Ag_2) are shown. From the band-gap values obtained, we can establish that the Ag_2 model is the one that best describes our experimental results, however, both Ag_1 and Ag_2 models will be analyzed. It is noted that the calculated band gaps are lower that experimental values, which is due to the known shortcoming of exchange-correction functional [35,80,87–89]. To further understand the composition and nature of the band structures, the total DOS of ACO and ACOZn and PDOS of Ag, Cr, O and Zn were calculated and are shown in Fig 18.

An analysis of the DOS of pure ACO (Fig. 18A) shows that the upper part of the VB is predominantly formed by the Ag 4*d* and O 2*p* orbitals, while the lower part of the CB is formed by the contribution of the p orbitals of the O atoms and the empty Cr 3*d* orbitals. Meanwhile, for the ACOZn systems, in both theoretical models (Fig. 18B and C), the top of the VB consists mainly of Ag $4dz^2$, $4dx^2 - y^2$ and $4dyz$ orbitals and O

$2p_z$ orbitals and the bottom of the CB has contributions of the Zn $4s$ orbitals, Cr $3d$ orbitals and O $2p_z$. The important contribution that Cr makes to the CB and his potential ability to lower down the bottom of the CB [15,76] is also evidenced in both models. However, in Ag_2 model is observed that Cr $3d$ states along with Zn $4s$ states shift toward lower energy that in Ag_1 causing a strong decreasing in the band gap. Inset of Figure 18C show the overlapping between Cr $3d$ and Zn $4s$ states. The decreasing of band gap observed in Ag_2 model could be caused by the structural change due to the formation of under-coordination [ZnO_4] clusters affecting Cr−O and Ag−O bond angles and distances.

Also, it is evidenced in Figs. 16B and 16C, that new electronic states located in the energy region corresponding to the band-gap of the material are created. These new electronic states are related to the structural changes and density of defects due to the [ZnO_6] or [ZnO_4] clusters presented in the substituted material.

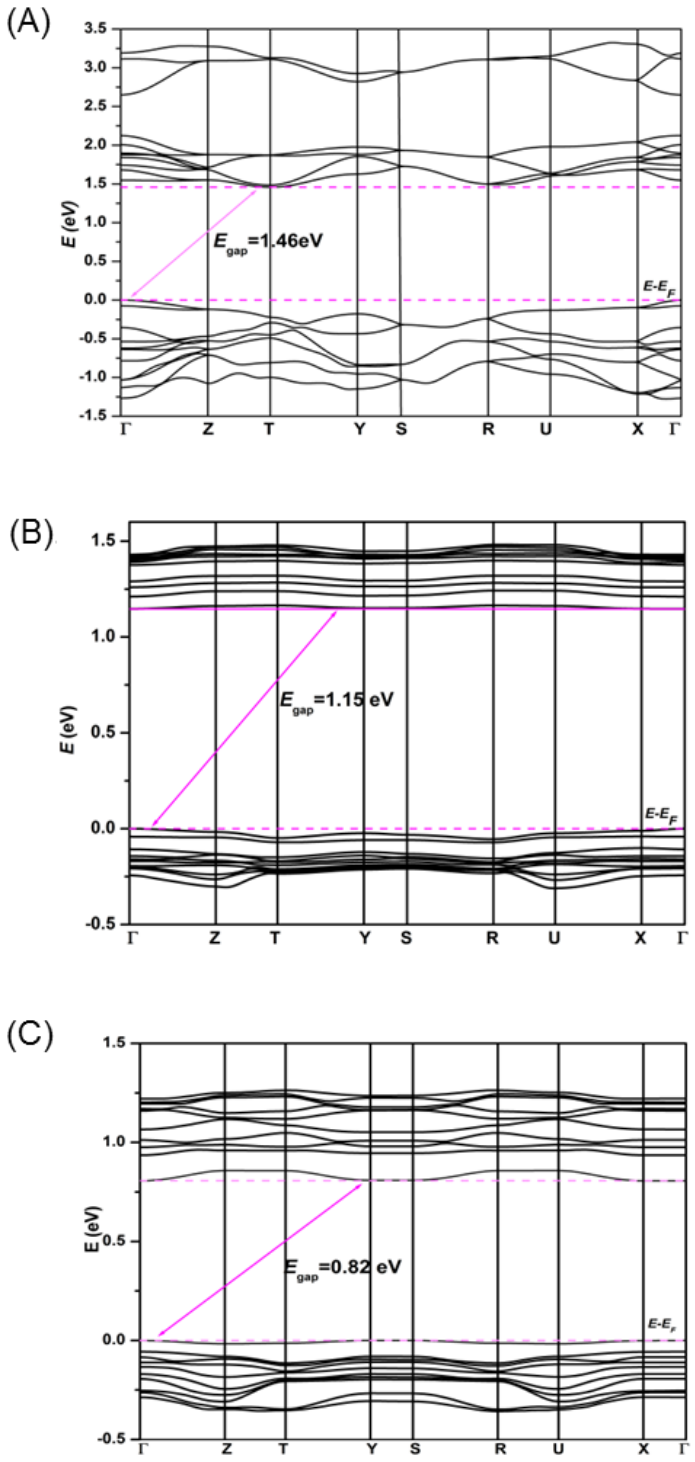

Fig.16. Band structures of (A) ACO, (B) ACOZn (Ag_1) and (C) ACOZn (Ag_2).

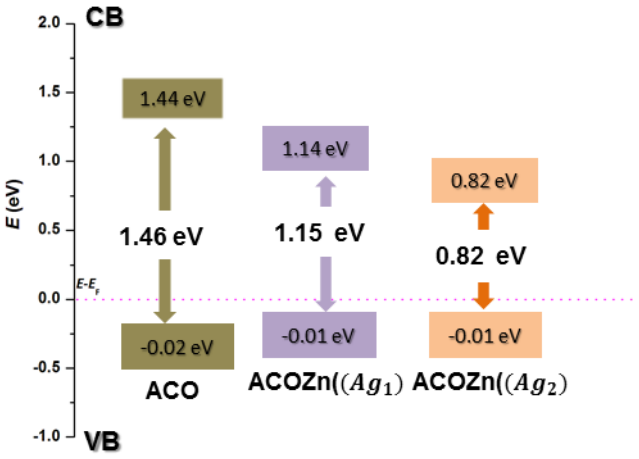

Fig.17. Band structure alignments for ACO, ACOZn (Ag_1) and ACOZn (Ag_2).

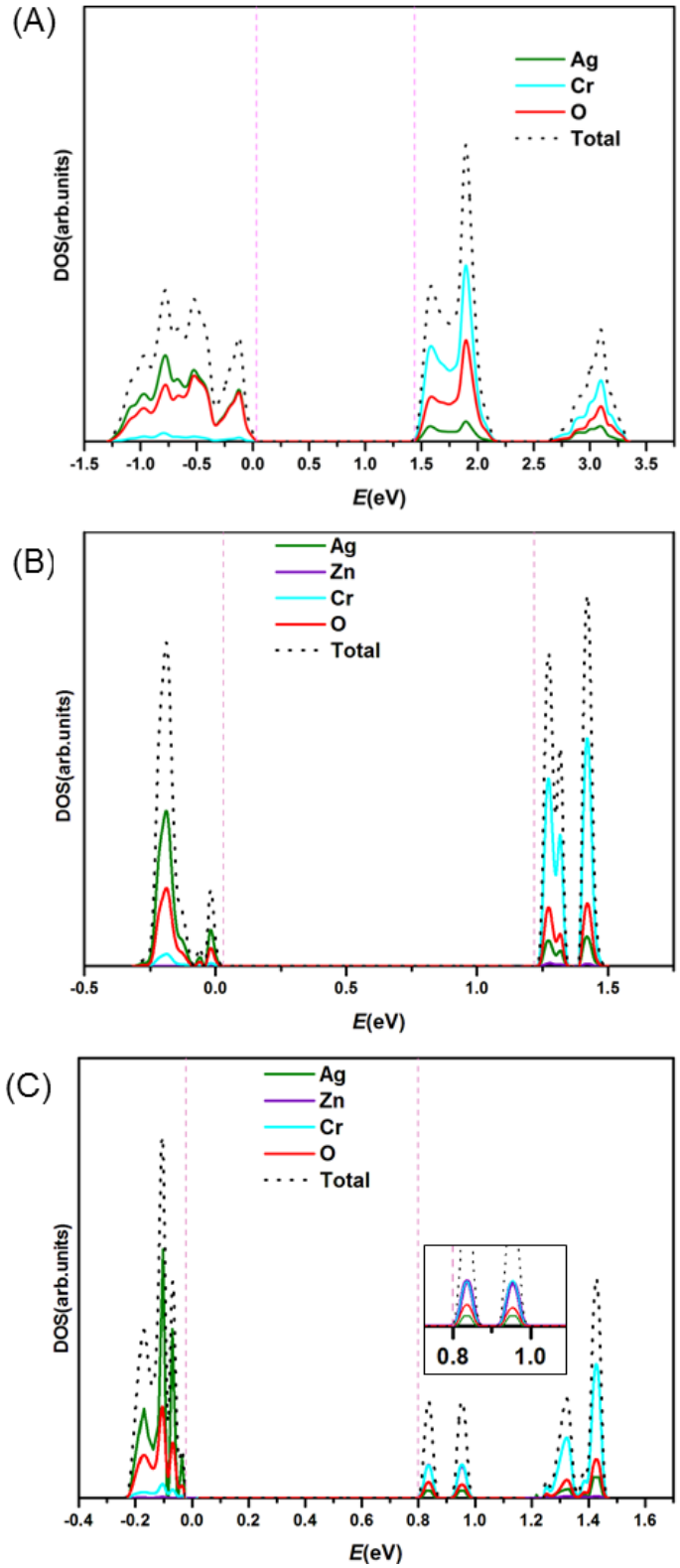

Fig.18. Density of states of (A) ACO, (B) ACOZn (Ag_1) and (C) ACOZn (Ag_2).

Bactericidal and fungicidal activities

The bactericidal and fungicidal capacities of the ACO, ACO1Zn, ACO2Zn and ACO4Zn samples were measured against MRSA and C. *albicans* standards strains. All

of the samples showed antimicrobial activity against both microorganisms, and the efficacy followed the order: ACO < ACO1Zn < ACO4Zn < ACO2Zn.

Bactericidal (MBC), fungicidal (MFC), inhibitory (MIC) and sub inhibitory (sub-MIC) concentrations are shown in Fig. 19. Although the samples showed the same behavior for both microorganisms, the values found for MBC and MFC were quite different. While for MRSA, the MBC was 31.25 μg/mL for the ACO2Zn sample, the same sample had CFM of 3.9 μg/mL for *C. albicans*.

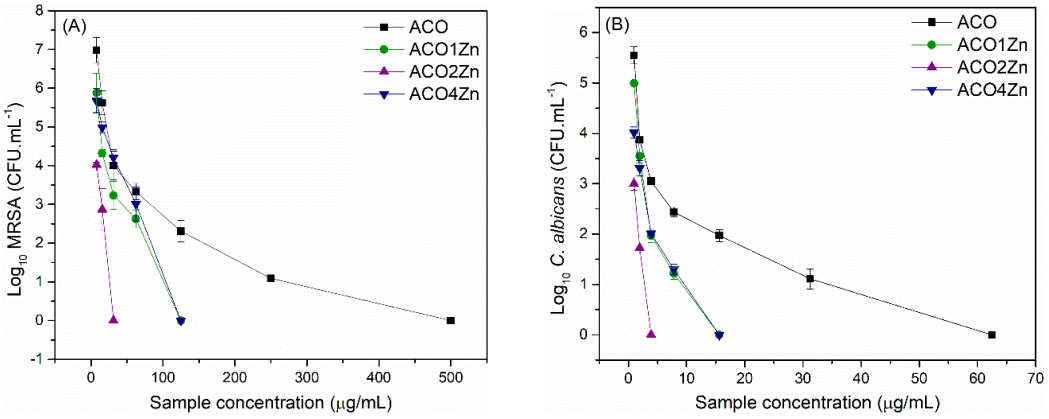

Fig. 19. Antimicrobial activity of the synthesized compounds against (A) MRSA and (B) *C. albicans.*

When isolated, zinc and silver are known to show antimicrobial activity. With the addition of Zn in the matrix, there was a significant increase in antimicrobial activity against bacteria and fungus, and this was directly proportional to the amount of the incorporated Zn up to the concentration of 2%. Improvement in antibacterial efficiency is due to the synergistic effect between Zn and the Ag particles [90]. Additionally, Cr present in the samples also has strong antibacterial activity, causing disruption of amino acid and DNA synthesis, and leading to cell death [91].

In addition to the synergistic effect between the components, the reduction of the ACO2Zn band gap demonstrates the possibility of facilitated excitation for this sample, which may contribute to the catalytic mechanisms involved in antimicrobial activity [91]. Experiments using reactive species scavengers showed that O_2' and h• are the main players in the photocatalytic capacity of the material. With the band gap reduction, O_2H* production becomes easier, increasing the antimicrobial efficiency. The formation of reactive O_2H* species is responsible for damage to microorganisms.

It was observed that the efficacies of the synthesized materials vary according to the tested microorganism. The differences found between the minimum bactericidal/fungicidal concentrations are due to morphological differences between microbial cells. The *C. albicans* cell wall is composed of complex glucose polymers, N-acetylglucosamine chains and cell wall mannoproteins. Together with chitin, glucans form a rigid and complex skeleton responsible for the morphology and physical resistance of the fungal cell [92]. Methicillin-resistant *S. aureus* bacteria has cell walls that are composed of a cytoplasmic membrane and a thick and overlying peptidoglycan network composed of repeated units of polymerized disaccharide-multipeptide. Since the cell wall is crucial for the mechanical and chemical integrity of cells, because it protects them from the external environment and stress, all of the above-mentioned differences between the microorganisms may have contributed to the higher activity of the microcrystals against the *C. albicans* microorganism relative to that against *S. aureus* bacteria. Knowledge of microbial cell morphology along with the investigation of the characteristics of the tested materials is essential for understanding the mechanisms involved in microbial elimination. In particular, these data are essential for the development of functional materials with biological properties.

Conclusions

In summary, efficient multifunction materials (ACOxZn, x = 1%, 2%, and 4%) that act as a visible-light-driven photocatalyst and have antimicrobial activity have been successfully obtained, for the first time, *via* a facile co-precipitation method due to the cation exchange of zinc with silver in the ACO lattice. XRD results confirmed the crystallinity of the samples without deleterious phases, confirming long-range order, whereas the results for the Raman vibrational modes showed short-range structural disorder. XPS and ICP OES analyses confirmed that the materials were pure and contain Zn^{2+} cations. UV-vis DRS and PL emission spectra were in agreement with the results of PC analysis. The PC and bactericidal and fungicidal activities were enhanced due to Zn^{2+} cations, which increased with increasing Zn^{2+} content until the optimal Zn^{2+} concentration of 2% was attained. The experimental and theoretical results, supported by first-principles calculations at the DFT level, were discussed in terms of the structural and electronic order/disorder effects of the materials and their surface energies. These results confirm the efficacy of Zn^{2+} insertion into the matrix as a breakthrough strategy for improving material properties and applications.

Conflicts of interest

There are no conflicts to declare.

Acknowledgments

The authors are grateful for the support of the Brazilian research financing institution: CNPq (grant no.150937/2018-0) and FAPESP (grant no.13/07296-2). They also wish to thank Rorivaldo Camargo (LIEC, UFSCar), Prof. Yara Galvão Gobato (DF, UFSCar), Prof. Joaquim de Araújo Nobrega (Grupo de Análise Instrumental Aplicada, DQ, UFSCar) and Lucimar Lopes Fialho (Grupo de Análise Instrumental Aplicada, DQ, UFSCar) for technical and scientific contributions. J.A. acknowledges Universitat Jaume I for project UJI-B2016-25, Generalitat Valenciana for project Prometeo II/2014/022, ACOMP/2014/270, and ACOMP/2015/1202, and Ministerio de Economia y Competitividad (Spain) project CTQ2015-65207-P, and Ministerio de Ciencia, Innovación y Universidades (Spain) project PGC2018-094417-B-I00 for supporting this research financially.

References

1. Yang, Y. *et al.* Facile synthesis of ZnO/Ag nanocomposites with enhanced photocatalytic properties under visible light. *Mater. Lett.* **180**, 97–100 (2016).

2. Tong, H. *et al.* Nano-photocatalytic materials: Possibilities and challenges. *Adv. Mater.* **24**, 229–251 (2012).

3. Trench, A. B. *et al.* Connecting structural, optical, and electronic properties and photocatalytic activity of Ag 3 PO 4 :Mo complemented by DFT calculations. *Appl. Catal. B Environ.* **238**, 198–211 (2018).

4. Liang, Z. *et al.* Full solar spectrum photocatalytic oxygen evolution by carbon-coated TiO2 hierarchical nanotubes. *Appl. Catal. B Environ.* **243**, 711–720 (2019).

5. Li, Y. *et al.* Boosting the Photocatalytic Ability of g-C3N4 for Hydrogen Production by Ti3C2 MXene Quantum Dots. *ACS Appl. Mater. Interfaces* **11**, 41440–41447 (2019).

6. Zhang, X., Lv, X., Bi, F., Lu, G. & Wang, Y. Highly efficient Mn2O3 catalysts derived from Mn-MOFs for toluene oxidation: The influence of MOFs precursors. *Mol. Catal.* **482**, (2020).

7. Wang, L., Yin, G., Yang, Y. & Zhang, X. Enhanced CO oxidation and toluene oxidation on CuCeZr catalysts derived from UiO-66 metal organic frameworks. *React. Kinet. Mech. Catal.* **128**, 193–204 (2019).

8. Che, Y. *et al.* Bio-inspired Z-scheme g-C 3 N 4 /Ag 2 CrO 4 for efficient visible-light photocatalytic hydrogen generation. *Sci. Rep.* **8**, 1–12 (2018).

9. Luo, J. *et al.* Facile fabrication and enhanced visible-light photocatalytic activity of In2O3/Ag2CrO4composites. *RSC Adv.* **6**, 52627–52635 (2016).

10. Xu, D., Cheng, B., Wang, W., Jiang, C. & Yu, J. Ag2CrO4/g-C3N4/graphene oxide ternary nanocomposite Z-scheme photocatalyst with enhanced CO2 reduction activity. *Appl. Catal. B Environ.* **231**, 368–380 (2018).

11. Pirhashemi, M. & Habibi-Yangjeh, A. Novel ZnO/Ag2CrO4 nanocomposites with n–n heterojunctions as excellent photocatalysts for degradation of different pollutants under visible light. *J. Mater. Sci. Mater. Electron.* **27**, 4098–4108 (2016).

12. Luo, J. *et al.* Enhanced photodegradation activity of methyl orange over Ag2CrO4/SnS2 composites under visible light irradiation. *Mater. Res. Bull.* **77**, 291–299 (2016).

13. Shi, L., Liang, L., Wang, F., Liu, M. & Sun, J. Ag2CrO4 nanoparticles loaded on two-dimensional large surface area graphite-like carbon nitride sheets: Simple synthesis and excellent photocatalytic performance. *Dalt. Trans.* **45**, 5815–5824 (2016).

14. Liu, Z. *et al.* Silver chromate modified sulfur doped graphitic carbon nitride microrod composites with enhanced visible-light photoactivity towards organic pollutants degradation. *Compos. Part B Eng.* **173**, 106918 (2019).

15. Ouyang, S. *et al.* Correlation of crystal structures, electronic structures, and photocatalytic properties in a series of Ag-based oxides: AgAlO2, AgCrO2, and Ag2CrO4. *J. Phys. Chem. C* **112**, 3134–3141 (2008).

16. Liu, Y., Yu, H., Cai, M. & Sun, J. Microwave hydrothermal synthesis of Ag 2 CrO 4 photocatalyst for fast degradation of PCP-Na under visible light irradiation.

Catal. Commun. **26**, 63–67 (2012).

17. Brunetti, V., Villullas, H. M. & López Teijelo, M. Anodic film formation on silver in solutions containing chromate. *Electrochim. Acta* **44**, 2843–2851 (1999).

18. Kant, K. Condition of silver chromate in different media. *Kolloid-Zeitschrift Zeitschrift für Polym.* **190**, 47–49 (1963).

19. Kant, K. Conditions of the Formation of Yellow Sol of Silver Chromate. *Kolloid-Zeitschrift Zeitschrift für Polym.* **190**, 44–47 (1962).

20. Howard, J. R. & Nancollas, G. H. The Crystallization of Silver Chromate in Aqueous Solutions. **6**, 1449–1454 (1970).

21. Howard, J. R. & Nancollas, G. H. Crystallization of Silver Chromate. *Nature* **176**, 1955 (1955).

22. Li, Y. L. *et al.* Investigating the influence of a CrO 42− /Cr 2 O 72− template in the formation of a series of silver-chalcogenide clusters. *New J. Chem.* **43**, 115–120 (2019).

23. Macedo, N. G. *et al.* Tailoring the Bactericidal Activity of Ag Nanoparticles/α-Ag 2 WO 4 Composite Induced by Electron Beam and Femtosecond Laser Irradiation: Integration of Experiment and Computational Modeling . *ACS Appl. Bio Mater.* **2**, 824–837 (2019).

24. Doster, J. *et al.* Tailoring the surface plasmon resonance of embedded silver nanoparticles by combining nano- and femtosecond laser pulses. *Appl. Phys. Lett.* **104**, (2014).

25. Lemire, J. A., Harrison, J. J. & Turner, R. J. Antimicrobial activity of metals: Mechanisms, molecular targets and applications. *Nat. Rev. Microbiol.* **11**, 371–384 (2013).

26. Longo, V. M. *et al.* Potentiated electron transference in α-Ag2WO4 microcrystals with Ag nanofilaments as microbial agent. *J. Phys. Chem. A* **118**, 5769–5778 (2014).

27. De Foggi, C. C. *et al.* Tuning the morphological, optical, and antimicrobial

properties of α-Ag2WO4 microcrystals using different solvents. *Cryst. Growth Des.* **17**, 6239–6246 (2017).

28. Foggi, C. C. *et al.* Synthesis and evaluation of A-Ag2WO4 as novel antifungal agent. *Chem. Phys. Lett.* **674**, 125–129 (2017).

29. Assis, M. *et al.* Towards the scale-up of the formation of nanoparticles on α-Ag2WO4 with bactericidal properties by femtosecond laser irradiation. *Sci. Rep.* **8**, 1–11 (2018).

30. Machado, T. R. *et al.* From Complex Inorganic Oxides to Ag-Bi Nanoalloy: Synthesis by Femtosecond Laser Irradiation. *ACS Omega* **3**, 9880–9887 (2018).

31. Fabbro, M. T. *et al.* Synthesis, antifungal evaluation and optical properties of silver molybdate microcrystals in different solvents: A combined experimental and theoretical study. *Dalt. Trans.* **45**, 10736–10743 (2016).

32. Oliveira, C. A. *et al.* Well-designed β-Ag 2 MoO 4 crystals with photocatalytic and antibacterial activity. *Mater. Des.* **115**, 73–81 (2017).

33. De Oliveira, R. C. *et al.* Mechanism of Antibacterial Activity via Morphology Change of α-AgVO 3 : Theoretical and Experimental Insights. *ACS Appl. Mater. Interfaces* **9**, 11472–11481 (2017).

34. Silva, G. S. *et al.* Theoretical and Experimental Insight on Ag2CrO4 Microcrystals: Synthesis, Characterization, and Photoluminescence Properties. *Inorg. Chem.* **55**, 8961–8970 (2016).

35. Fabbro, M. T. *et al.* Understanding the formation and growth of Ag nanoparticles on silver chromate induced by electron irradiation in electron microscope: A combined experimental and theoretical study. *J. Solid State Chem.* **239**, 220–227 (2016).

36. P. S., L. *et al.* Laser and electron beam-induced formation of Ag/Cr structures on Ag 2 CrO 4. *Phys. Chem. Chem. Phys.* **21**, 6101–6111 (2019).

37. Pereira, P. F. S. *et al.* α-Ag2-2xZnxWO4 ($0 \leq \times \leq 0.25$) Solid Solutions: Structure, Morphology, and Optical Properties. *Inorg. Chem.* **56**, 7360–7372 (2017).

38. Dovesi, R. *et al.* Quantum-mechanical condensed matter simulations with CRYSTAL. *Wiley Interdiscip. Rev. Comput. Mol. Sci.* **8**, 1–36 (2018).

39. Erba, A., Baima, J., Bush, I., Orlando, R. & Dovesi, R. Large-Scale Condensed Matter DFT Simulations: Performance and Capabilities of the CRYSTAL Code. *J. Chem. Theory Comput.* **13**, 5019–5027 (2017).

40. Perdew, J. P., Burke, K. & Ernzerhof, M. Generalized Gradient Approximation Made Simple. **77**, 3865–3868 (1996).

41. Ruiz, E., Llunell, M. & Alemany, P. Calculation of exchange coupling constants in solid state transition metal compounds using localized atomic orbital basis sets. *J. Solid State Chem.* **176**, 400–411 (2003).

42. Catti, M., Sandrone, G., Valerio, G. & Dovesi, R. Electronic, magnetic and crystal structure of Cr2O3 by theoretical methods. *J. Phys. Chem. Solids* **57**, 1735–1741 (1996).

43. Baima, J., Erba, A., Rérat, M., Orlando, R. & Dovesi, R. Beryllium oxide nanotubes and their connection to the flat monolayer. *J. Phys. Chem. C* **117**, 12864–12872 (2013).

44. Narth, C. *et al.* Scalable improvement of SPME multipolar electrostatics in anisotropic polarizable molecular mechanics using a general short-range penetration correction up to quadrupoles. *J. Comput. Chem.* **37**, 494–505 (2016).

45. Rai, D. P. *et al.* Erratum: Study of the enhanced electronic and thermoelectric (TE) properties of ZrxHf1-x-yTayNiSn: A first principles study (RSC Advances (2015) 5 (95353-95359)). *RSC Adv.* **6**, 13358 (2016).

46. Rai, D. P. *et al.* Spin-induced transition metal (TM) doped SnO2 a dilute magnetic semiconductor (DMS): A first principles study. *J. Phys. Chem. Solids* **120**, 104–108 (2018).

47. Hackert, M. L. & Jacobson, R. A. The crystal structure of silver chromate. *J. Solid State Chem.* **3**, 364–368 (1971).

48. Coelho, A. A. TOPAS and TOPAS-Academic: An optimization program integrating computer algebra and crystallographic objects written in C++: An. *J.*

Appl. Crystallogr. **51**, 210–218 (2018).

49. Ortiz, A. L., F.L. Cumbrera, F. Sanchez-Bajo, F. Guiberteau & R. Caruso. Fundamental parameters approach in the Rietveld method: A study of the stability of results versus the accuracy of the instrumental profile. *J. Eur. Ceram. Soc.* **20**, 1845–1851 (2000).

50. Balzar, D. & Ledbetter, H. Voigt-function modeling in Fourier analysis of size- and strain-broadened X-ray diffraction peaks. *J. Appl. Crystallogr.* **26**, 97–103 (1993).

51. Toby, B. H. R factors in Rietveld analysis: How good is good enough? *Powder Diffr.* **21**, 67–70 (2008).

52. Momma, K. & Izumi, F. VESTA 3 for three-dimensional visualization of crystal, volumetric and morphology data. *J. Appl. Crystallogr.* **44**, 1272–1276 (2011).

53. Momma, K. & Izumi, F. VESTA : a three-dimensional visualization system for electronic and structural analysis . *J. Appl. Crystallogr.* **41**, 653–658 (2008).

54. Pereira, W. da S. *et al.* Influence of Cu substitution on the structural ordering, photocatalytic activity and photoluminescence emission of Ag 3-2x Cu x PO 4 powders. *Appl. Surf. Sci.* **440**, 61–72 (2018).

55. Cavalcante, L. S. *et al.* Cluster coordination and photoluminescence properties of α-Ag <inf>2</inf>WO <inf>4</inf> microcrystals. *Inorg. Chem.* **51**, (2012).

56. Andrés, J., Gracia, L., Gouveia, A. F., Ferrer, M. M. & Longo, E. Effects of surface stability on the morphological transformation of metals and metal oxides as investigated by first-principles calculations. *Nanotechnology* **26**, (2015).

57. Botelho, G., Andres, J., Gracia, L., Matos, L. S. & Longo, E. Photoluminescence and Photocatalytic Properties of Ag3PO4Microcrystals: An Experimental and Theoretical Investigation. *Chempluschem* **81**, 202–212 (2016).

58. Bomio, M. R. D. *et al.* Toward understanding the photocatalytic activity of PbMoO4 powders with predominant (111), (100), (011), and (110) facets. A combined experimental and theoretical study. *J. Phys. Chem. C* **117**, 21382–21395 (2013).

59. Fabbro, M. T. *et al.* Identifying and rationalizing the morphological, structural, and optical properties of β-Ag 2 MoO 4 microcrystals, and the formation process of Ag nanoparticles on their surfaces: Combining experimental data and first-principles calculations. *Sci. Technol. Adv. Mater.* **16**, 65002 (2015).

60. Longo, V. M. *et al.* A joint experimental and theoretical study on the nanomorphology of CaWO4 crystals. *J. Phys. Chem. C* **115**, 20113–20119 (2011).

61. Oliveira, M. C. *et al.* Synthesis and morphological transformation of BaWO4 crystals: Experimental and theoretical insights. *Ceram. Int.* **42**, 10913–10921 (2016).

62. Ribeiro, R. A. P., Lacerda, L. H. S., Longo, E., Andrés, J. & de Lazaro, S. R. Towards enhancing the magnetic properties by morphology control of ATiO 3 (A = Mn, Fe, Ni) multiferroic materials. *J. Magn. Magn. Mater.* **475**, 544–549 (2019).

63. Zhu, J., Fan, H., Sun, J. & Ai, S. Anion-exchange precipitation synthesis of α-Ag2WO 4/Zn-Cr layered double hydroxides composite with enhanced visible-light-driven photocatalytic activity. *Sep. Purif. Technol.* **120**, 134–140 (2013).

64. Lin, Z. *et al.* Electronic Reconstruction of α-Ag_2WO_4 Nanorods for Visible-Light Photocatalysis. *ACS Nano* **9**, 7256–7265 (2015).

65. Wang, Z. *et al.* Hollow ZSM-5 zeolite encapsulated Ag nanoparticles for SO2-resistant selective catalytic oxidation of ammonia to nitrogen. *Sep. Purif. Technol.* **209**, 1016–1026 (2019).

66. Zhou, M. *et al.* High-Performance Ag-Cu Nanoalloy Catalyst for the Selective Catalytic Oxidation of Ammonia. *ACS Appl. Mater. Interfaces* **11**, 46875–46885 (2019).

67. Zhang, X. *et al.* High and stable catalytic activity of Ag/Fe2O3 catalysts derived from MOFs for CO oxidation. *Mol. Catal.* **447**, 80–89 (2018).

68. Catto, A. C. *et al.* Improving the ozone gas-sensing properties of CuWO 4 nanoparticles. *J. Alloys Compd.* **748**, 411–417 (2018).

69. Zhang, C. *et al.* Zeolitic acidity as a promoter for the catalytic oxidation of toluene

over MnO x /HZSM-5 catalysts. *Catal. Today* **327**, 374–381 (2019).

70. Zhang, C. *et al.* LaMnO3 perovskites via a facile nickel substitution strategy for boosting propane combustion performance. *Ceram. Int.* **46**, 6652–6662 (2020).

71. Tao, J. *et al.* Investigation of growth characteristics, compositions, and properties of atomic layer deposited amorphous Zn-doped Ga2O3 films. *Appl. Surf. Sci.* **476**, 733–740 (2019).

72. Liu, H. R. *et al.* Worm-like Ag/ZnO core-shell heterostructural composites: Fabrication, characterization, and photocatalysis. *J. Phys. Chem. C* **116**, 16182–16190 (2012).

73. Zhang, X. *et al.* Effects of Ag loading on structural and photocatalytic properties of flower-like ZnO microspheres. *Appl. Surf. Sci.* **391**, 476–483 (2017).

74. Clark, R. J. H. & Dines, T. J. Raman, Resonance Raman, and Infrared Spectroscopic Study of Silver(I) Chromate. *Inorg. Chem.* **21**, 3585–3588 (1982).

75. Xu, D., Cheng, B., Cao, S. & Yu, J. Enhanced photocatalytic activity and stability of Z-scheme Ag2CrO4-GO composite photocatalysts for organic pollutant degradation. *Appl. Catal. B Environ.* **164**, 380–388 (2015).

76. Santamaría-Pérez, D. *et al.* Phase behavior of Ag2CrO4 under compression: Structural, vibrational, and optical properties. *J. Phys. Chem. C* **117**, 12239–12248 (2013).

77. Nogueira, A. E., Oliveira, J. A., da Silva, G. T. S. T. & Ribeiro, C. Insights into the role of CuO in the CO 2 photoreduction process. *Sci. Rep.* **9**, 41598 (2019).

78. Wood, D. L. & Tauc, J. Weak absorption tails in amorphous semiconductors. *Phys. Rev. B* **5**, 3144–3151 (1972).

79. Philips-Invernizzi, B. Bibliographical review for reflectance of diffusing media. *Opt. Eng.* **40**, 1082 (2002).

80. Zhang, J., Yu, W., Liu, J. & Liu, B. Illustration of high-active Ag 2 CrO 4 photocatalyst from the first-principle calculation of electronic structures and carrier effective mass. *Appl. Surf. Sci.* **358**, 457–462 (2015).

81. Xu, D. *et al.* Photocatalytic activity of Ag2MO4 (M = Cr, Mo, W) photocatalysts. *J. Mater. Chem. A* **3**, 20153–20166 (2015).

82. Fan, H. *et al.* Novel Ag 2 CrO 4 /Bi 2 O 2 CO 3 heterojunction: Simple preparation, wide visible-light absorption band and excellent photocatalytic activity. *Chem. Phys.* **517**, 60–66 (2019).

83. Guettaï, N. & Ait Amar, H. Photocatalytic oxidation of methyl orange in presence of titanium dioxide in aqueous suspension. Part I: Parametric study. *Desalination* **185**, 427–437 (2005).

84. Zhu, L. *et al.* Fabrication of AgBr/Ag 2 CrO 4 composites for enhanced visible-light photocatalytic activity. *Ceram. Int.* **41**, 12509–12513 (2015).

85. Deng, Y. *et al.* Facile fabrication of a direct Z-scheme Ag2CrO4/g-C3N4 photocatalyst with enhanced visible light photocatalytic activity. *J. Mol. Catal. A Chem.* **421**, 209–221 (2016).

86. Kushwaha, A. K., Uğur, Akbudak, S. & Uğur, G. Investigation of structural, elastic, electronic, optical and vibrational properties of silver chromate spinels: Normal (CrAg2O4) and inverse (Ag2CrO4). *J. Alloys Compd.* **704**, 101–108 (2017).

87. Xu, D., Cao, S., Zhang, J., Cheng, B. & Yu, J. Effects of the preparation method on the structure and the visible-light photocatalytic activity of Ag2CrO4. *Beilstein J. Nanotechnol.* **5**, 658–666 (2014).

88. Lin, S., Huang, J. & Ye, X. Stability and electronic structure of iron nanoparticle anchored on defective hexagonal boron nitrogen nanosheet: A first-principle study. *Appl. Surf. Sci.* **320**, 237–243 (2014).

89. Perdew, J. P. & Levy, M. Physical content of the exact kohn-sham orbital energies: Band gaps and derivative discontinuities. *Phys. Rev. Lett.* **51**, 1884–1887 (1983).

90. Peng, J., Zhan, P., Deng, R., Zhang, Y. & Xie, X. Facile preparation, spectral property and application of Ag/ZnO nanocomposites. *Res. Chem. Intermed.* **45**, 4637–4651 (2019).

91. Vijayalakshmi, K. & Sivaraj, D. Enhanced antibacterial activity of Cr doped ZnO

nanorods synthesized using microwave processing. *RSC Adv.* **5**, 68461–68469 (2015).

92. Kapteyn, J. C. *et al.* The cell wall architecture of Candida albicans wild-type cells and cell wall-defective mutants. *Mol. Microbiol.* **35**, 601–611 (2000).